

---

This manuscript has been submitted for publication in *Frontiers in Earth Science*. Please note that, this is the peer-reviewed manuscript which is currently provisionally accepted. The final version of this manuscript will be available via the ‘Peer-reviewed Publication DOI’ link on this webpage.

---

**GARPOS: analysis software for the GNSS-A seafloor positioning with simultaneous estimation of sound speed structure**

**Shun-ichi Watanabe, Tadashi Ishikawa, Yusuke Yokota, Yuto Nakamura**

# GARPOS: analysis software for the GNSS-A seafloor positioning with simultaneous estimation of sound speed structure

1 Shun-ichi Watanabe<sup>1\*</sup>, Tadashi Ishikawa<sup>1</sup>, Yusuke Yokota<sup>2</sup>, Yuto Nakamura<sup>1</sup>

2 <sup>1</sup>Hydrographic and Oceanographic Department, Japan Coast Guard, 3-1-1, Kasumigaseki, Chiyoda-  
3 ku, Tokyo, Japan

4 <sup>2</sup>Institute of Industrial Science, University of Tokyo, 4-6-1, Komaba, Meguro-ku, Tokyo, Japan

5 \* **Correspondence:**

6 Shun-ichi Watanabe

7 s-watanabe@jodc.go.jp

8

9 **Keywords: GNSS-A, seafloor geodesy, sound speed structure, GNSS-A methodology, GNSS-A**  
10 **oceanography**

## 11 **Abstract**

12 Global Navigation Satellite System – Acoustic ranging combined seafloor geodetic technique  
13 (GNSS-A) has extended the geodetic observation network into the ocean. The key issue for analyzing  
14 the GNSS-A data is how to correct the effect of sound speed variation in the seawater. We  
15 constructed a generalized observation equation and developed a method to directly extract the  
16 gradient sound speed structure by introducing appropriate statistical properties in the observation  
17 equation, especially the data correlation term. In the proposed scheme, we calculate the posterior  
18 probability based on the empirical Bayes approach using the Akaike's Bayesian Information  
19 Criterion (ABIC) for model selection. This approach enabled us to suppress the overfitting of sound  
20 speed variables and thus to extract simpler sound speed field and stable seafloor positions from the  
21 GNSS-A dataset. The proposed procedure is implemented in the Python-based software "GARPOS"  
22 (GNSS-Acoustic Ranging combined POSitioning Solver).

## 23 **1 Introduction**

### 24 **1.1 Basic configurations of the GNSS-A observation**

25 Precise measurements of seafloor position in the global reference frame opens the door to the  
26 "global" geodesy in the true sense of the word. It extended the observation network for crustal  
27 deformation into the ocean and has revealed the tectonic processes in the subduction zone including  
28 megathrust earthquakes (e.g., Bürgmann and Chadwell, 2014; Fujimoto, 2014, for review). Many  
29 findings have been reported especially in the northwestern Pacific along the Nankai Trough (e.g.,  
30 Yokota et al., 2016; Yasuda et al., 2017; Yokota and Ishikawa, 2020), and the Japan Trench (e.g.,  
31 Sato et al., 2011; Kido et al., 2011; Watanabe et al., 2014; Tomita et al., 2015; Tomita et al., 2017).  
32 These achievements owe to the development of GNSS-A (Global Navigation Satellite System –  
33 Acoustic ranging combined) seafloor positioning technique, proposed by Spiess (1980).

34 Observers can take various ways to design the GNSS-A observation for the positioning of the  
35 seafloor benchmark. They have to solve the difficulties not only in the technical realizations of  
36 GNSS-A subcomponents such as the acoustic ranging and the kinematic GNSS positioning, but also  
37 in designing the observation configurations and analytical models to resolve the strongly correlated  
38 parameters. For example, because the acoustic ranging observations are performed only on the sea  
39 surface, the sound speed perturbations and the depth of the benchmark are strongly correlated.

40 In the very first attempt for the realization, Spiess et al. (1998) derived horizontal displacement using  
41 a stationary sea-surface unit which was approximately placed on the horizontal center of the array of  
42 multiple seafloor mirror transponders. They determined the relative positions and depths of the  
43 transponders in advance. The relative horizontal positions of the sea-surface unit to the transponder  
44 array can be determined by acoustic ranging data, to be compared with its global positions  
45 determined by space geodetic technique. In this “stationary” GNSS-A configuration, the temporal  
46 variation of sound speed is less likely to affect the apparent horizontal position under the assumption  
47 that the sound speed structure is horizontally stratified. Inversely, comparing the residuals of acoustic  
48 travel time from multiple transponders, Osada et al. (2003) succeeded in estimating the temporal  
49 variation of sound speed from the acoustic data. Kido et al. (2008) modified the expression to  
50 validate the stationary configuration for a loosely tied buoy even in the case where the sound speed  
51 has spatial variations. The stationary GNSS-A configuration is applied mainly by the groups in the  
52 Scripps Institution of Oceanography (e.g., Gagnon et al., 2005; Chadwell and Spiess, 2008) and in  
53 the Tohoku University (e.g., Fujimoto, 2014; Tomita et al., 2015; Tomita et al., 2017).

54 On the other hand, Obana et al. (2000) and Asada and Yabuki (2001) took a “move-around”  
55 approach where the 3-dimensional position of single transponder can be estimated by collecting the  
56 acoustic data from various relay points on the sea surface. Figure 1 shows the schematic image of  
57 move-around configuration. The move-around GNSS-A configuration is developed and practicalized  
58 mainly by the collaborative group of the Japan Coast Guard and the University of Tokyo, and the  
59 Nagoya University. Unlike the stationary configuration, the horizontal positions of transponders are  
60 vulnerable to bias errors of sound speed field. Fujita et al. (2006) and Ikuta et al. (2008) then  
61 developed the methods estimating both the positions and the temporal variations of sound speed.

62 Similar to the effects of distribution of the GNSS satellites on the positioning, well-distributed  
63 acoustic data is expected to decrease the bias errors of the estimated transponders’ positions in the  
64 move-around configuration. By implementing the sailing observations where the sea-surface unit  
65 sails over the transponder array to collect geometrically symmetric data, positioning accuracy and  
66 observation efficiency have improved (Sato et al., 2013; Ishikawa et al., 2020).

67 In order to enhance the stability of positioning, an assumption that the geometry of transponder array  
68 is constant over whole observation period is usually adopted (e.g., Matsumoto et al., 2008; Watanabe  
69 et al., 2014; Chen et al., 2018; Yokota et al., 2018). Misestimates of sound speed cause the positional  
70 biases parallel to the averaged acoustic-ray direction, which results in the distortion of the estimated  
71 array geometry. Constraining the array geometry contributes to reducing the bias error in the sound  
72 speed estimates and the transponders’ centroid position.

73 It should be noted that these two configurations are compatible under the adequate assumptions and  
74 constraints. Recently, the group in the Tohoku University uses not only the stationary but also the  
75 move-around observation data collected for determining the array geometry (Honscho and Kido,  
76 2017).

## 77 1.2 Recent improvements on GNSS-A analytical procedures

78 In the late 2010s, analytical procedures with the estimation of the spatial sound speed gradient for the  
 79 move-around configuration have been developed. In the earlier stage of the move-around GNSS-A  
 80 development, the spatial variations of sound speed were approximated as the temporal variations,  
 81 because most of the sound speed change are confined in the shallowest portion along the acoustic ray  
 82 paths (e.g., Watanabe and Uchida, 2016). Actually, Yokota et al. (2019) extracted the spatial gradient  
 83 of the sound speed in the shallow layer from the estimated temporal sound speed variation. However,  
 84 the smoothly modeled temporal variations cannot represent the transponder-dependent variation  
 85 which is caused by the sound speed gradient in the relatively deeper portion. Therefore, Yokota et al.  
 86 (2019) extracted the transponder-dependent correction term from the residuals of the results derived  
 87 by the conventional method of Fujita et al. (2006).

88 Yasuda et al. (2017) took a different approach where the sound speed structure shallower than 1000  
 89 m is assumed to be inclined in one direction due to the Kuroshio current flowing near their sites in  
 90 the offshore region south of Kii Peninsula, Japan. Because their model reflects the specific  
 91 oceanographic feature, the estimated parameters are easier to be interpreted than that of Yokota et al.  
 92 (2019) which has higher degree of freedom to extract the oceanographic features.

93 Meanwhile, Honsho et al. (2019) showed a more general expression for one-directional sound speed  
 94 gradient. As they mentioned, the gradient terms in their formulation correspond to the extracted  
 95 features in Yokota et al. (2019). The work by Honsho et al. (2019) showed the possibility to connect  
 96 all the GNSS-A configurations into a unified GNSS-A solver. However, due to the limitation in  
 97 resolving the general gradient structure, an additional constraint was taken for the practical  
 98 application, which is essentially the same formulation as Yasuda et al. (2017).

99 In this study, to overcome the limitation above, we propose a method to directly extract the gradient  
 100 sound speed structure by introducing appropriate statistical properties in the observation equation.  
 101 This paper first shows the reconstructed general observation equation for GNSS-A, in which only the  
 102 continuity of the sound speed field in time and space is assumed. The generalized formulation  
 103 approximately includes the practical solutions in the previous studies by Yokota et al. (2019), Yasuda  
 104 et al. (2017), and Honsho et al. (2019) as special cases. We then describe the analytical procedure to  
 105 derive the posterior probability based on the empirical Bayes approach using the Akaike's Bayesian  
 106 Information Criterion (ABIC; Akaike, 1980) for model selection. We obtain the solution which  
 107 maximizes the posterior probability under the empirically selected prior distribution. This is  
 108 implemented in the Python-based software "GARPOS" (GNSS-Acoustic Ranging combined  
 109 Positioning Solver; Watanabe et al., 2020a, available at <https://doi.org/10.5281/zenodo.3992688>).

## 110 2 Methodology

### 111 2.1 Positioning of sea-surface transducer

112 The key subcomponent of the GNSS-A is the global positioning of the transducer, generally realized  
 113 by GNSS observation. Whereas acoustic measurement determines the relative positions of the  
 114 seafloor transponders and the sea-surface transducer, GNSS plays a role to align them to the earth-  
 115 centered, earth-fixed (ECEF) coordinates such as the International Terrestrial Reference Frame  
 116 (ITRF). When the transducer's position,  $\mathbf{P}(t)$ , is determined in the GNSS's reference frame, a  
 117 realization of the ITRF, the global positions of transponders can be estimated.

118 It should be noted that the transponders' positions are generally a function of time, including the  
 119 solid earth tide as well as global and local crustal deformation (e.g., IERS Conventions, 2010). For  
 120 the purpose of detecting crustal deformation, it is better to determine the seafloor positions in the  
 121 solid-earth-tide-free coordinates. Because the observation area is limited to several-kilometers-width,  
 122 solid-earth-tide-free solutions can be obtained when the trajectory of the transducer is determined in  
 123 the solid-earth-tide-free coordinates. Hereafter, the positions are expressed in solid-earth-tide-free  
 124 coordinates in this paper.

125 In order to determine  $\mathbf{P}(t)$  in the ECEF coordinates, a set of GNSS antenna/receiver and a gyro  
 126 sensor should be mounted on the sea-surface unit. The positions of GNSS antenna,  $\mathbf{Q}(t)$ , can be  
 127 determined using any of appropriate kinematic GNSS solvers. The gyro sensor provides the attitude  
 128 of the sea-surface platform,  $\boldsymbol{\Theta}(t) = [\theta_r \ \theta_p \ \theta_h]^T$ , i.e., roll, pitch, and heading (Figure 2). Because  
 129 the attitude values are aligned to the local ENU coordinates, it is convenient to transform  $\mathbf{Q}(t)$  from  
 130 ECEF to local ENU coordinates, i.e.,  $\mathbf{Q}(t) = [Q_e \ Q_n \ Q_u]^T$ . Using the relative position of the  
 131 transducer to the GNSS antenna in the gyro's rectangular coordinate (called "ATD offset" hereafter;  
 132 Figure 2),  $\mathbf{M} = [M_r \ M_p \ M_h]^T$ , we obtain the transducer's position in the local ENU coordinates  
 133 as,

$$134 \quad \mathbf{P}(t) = \mathbf{Q}(t) + R(\boldsymbol{\Theta}(t))\mathbf{M}, \quad (1.1)$$

135 with,

$$136 \quad R(\boldsymbol{\Theta}) = \begin{bmatrix} 0 & 1 & 0 \\ 1 & 0 & 0 \\ 0 & 0 & -1 \end{bmatrix} \begin{bmatrix} \cos \theta_h & -\sin \theta_h & 0 \\ \sin \theta_h & \cos \theta_h & 0 \\ 0 & 0 & 1 \end{bmatrix} \begin{bmatrix} \cos \theta_p & 0 & \sin \theta_p \\ 0 & 1 & 0 \\ -\sin \theta_p & 0 & \cos \theta_p \end{bmatrix} \begin{bmatrix} 1 & 0 & 0 \\ 0 & \cos \theta_r & -\sin \theta_r \\ 0 & \sin \theta_r & \cos \theta_r \end{bmatrix}. \quad (1.2)$$

137 The ATD offset values should be measured before the GNSS-A observation.

## 138 2.2 Underwater acoustic ranging

139 Another key subcomponent is the technique to measure the acoustic travel time between the sea-  
 140 surface transducer and the seafloor transponders. The techniques for the precise ranging using  
 141 acoustic mirror-type transponders had been developed and practicalized in early studies (e.g., Spiess,  
 142 1980; Nagaya, 1995). Measuring round-trip travel time reduces the effect of advection of the media  
 143 between the instruments.

144 The round-trip travel time for the  $i$ th acoustic signal to the  $j$ th transponder,  $T_i$ , is calculated as a  
 145 function of the relative position of the transponder to the transducer and the 4-dimensional sound  
 146 speed field,  $V(e, n, u, t)$ , i.e.,

$$147 \quad T_i = T_i^c \left( \mathbf{P}(t_{i+}), \mathbf{P}(t_{i-}), \mathbf{X}_j, V(e, n, u, t) \right), \quad (2)$$

148 where  $t_{i+}$ ,  $t_{i-}$ , and  $\mathbf{X}_j$  are the transmitted and received time for the  $i$ th acoustic signal, and the  
 149 position of seafloor transponder numbered  $j$ , respectively. Note that  $j$  is a function of  $i$ .

150 Although the concrete expression is provided as the eikonal equation (e.g., Jensen et al., 2011; Sakic  
 151 et al., 2018), it requires much computational resources to numerically solve. When the sound speed  
 152 structure is assumed to be horizontally stratified, we can apply a heuristic approach based on the

153 Snell's law (e.g., Hovem, 2013), which has an advantage in computation time (e.g., Chadwell and  
 154 Sweeney, 2010; Sakic et al., 2018).

155 Therefore, we decomposed the 4-dimensional sound speed field into a horizontally stratified stationary  
 156 sound speed profile and a perturbation to obtain the following travel time expression:

$$157 \quad T_i^c \left( \mathbf{P}(t_{i+}), \mathbf{P}(t_{i-}), \mathbf{X}_j, V(e, n, u, t) \right) = \exp(-\gamma_i) \cdot \tau_i \left( \mathbf{P}(t_{i+}), \mathbf{P}(t_{i-}), \mathbf{X}_j, V_0(u) \right), \quad (3)$$

158 where  $\tau_i$  and  $V_0(u)$  denote the reference travel time and the reference sound speed profile,  
 159 respectively.  $V_0(u)$  is given as a piecewise linear function of height, so that the propagation length  
 160 along the radial component and the propagation time can be calculated for the given incidence angle  
 161 according to the Snell's law (e.g., Hovem, 2013; Sakic et al. 2018). The expression of the correction  
 162 coefficient,  $\exp(-\gamma_i)$ , is selected for the simplification in the following expansion. It represents the  
 163 discrepancy ratio of the actual travel time to the reference, which caused by the spatial and temporal  
 164 perturbations of the sound speed field.

165 In the right-hand side of equation 3,  $\gamma_i$  and  $\mathbf{X}_j$  are assigned as the estimator. Equation 1 gives the  
 166 transducer's position  $\mathbf{P}(t)$  as a function of the GNSS antenna's position  $\mathbf{Q}(t)$ , the attitude vector  
 167  $\boldsymbol{\theta}(t)$ , and the ATD offset  $\mathbf{M}$ . The time-independent parameter  $\mathbf{M}$  can be also assigned as the  
 168 estimator when the variation of the attitude value is large enough to resolve the parameter. Hence, the  
 169 reference travel time can be rewritten as  $\tau_i = \tau_i \left( \mathbf{X}_j, \mathbf{M} \middle| \mathbf{Q}(t), \boldsymbol{\theta}(t), V_0(u) \right)$ , where the variables on  
 170 the left and right sides of the vertical bar indicate the estimators and the observables, respectively.

### 171 2.3 Sound speed perturbation model

172 In seawater, sound speed is empirically determined as a function of temperature, salinity, and  
 173 pressure (e.g., Del Grosso, 1974). Because these variables strongly depend on the water depth, the  
 174 vertical variation of the sound speed is much larger than the horizontal variation in the observation  
 175 scale. Thus,  $|\gamma_i| \ll 1$  will be satisfied in most cases where the reference sound speed appropriately  
 176 represents the sound speed field. In such cases, the average sound speed along the actual ray path is  
 177 expressed as  $\bar{V}_0 + \delta V_i \sim \bar{V}_0 + \gamma_i \bar{V}_0$ , where  $\bar{V}_0$  denotes the average sound speed of the reference  
 178 profile.

179 Recalling that the sound speed field is continuous and usually smooth in time and space within the  
 180 observation scale, we can introduce a scalar field which is continuous with time and acoustic  
 181 instruments' positions, i.e.,  $\Gamma(t, \mathbf{P}, \mathbf{X})$ , from which the correction coefficient is extracted. Because the  
 182 temporal variation of the sound speed structure is small during the travel of the acoustic signal and is  
 183 usually concentrated in the shallower portion of the sea,  $\gamma_i$  is approximated by the average of the  
 184 transmission and the reception times, i.e.,  $\gamma_i \equiv \frac{1}{2} \sum_{l=i+, i-} \Gamma(t_l, \mathbf{P}(t_l), \mathbf{X}_j)$ . The function  $\Gamma(t, \mathbf{P}, \mathbf{X})$  can  
 185 be called the sound speed perturbation model.

186 For simplification, we put the sound speed perturbation model as time-varying linear spatial function  
 187 in space as follows:

$$188 \quad \Gamma(t, \mathbf{P}, \mathbf{X}) \equiv \alpha_0(t) + \boldsymbol{\alpha}_1(t) \cdot \frac{\mathbf{P}}{L^*} + \boldsymbol{\alpha}_2(t) \cdot \frac{\mathbf{X}}{L^*}, \quad (4)$$

189 where  $L^*$  indicates the characteristic length of the observation site (typically in several kilometers).  
 190  $\alpha_0(t)$ ,  $\alpha_1(t)$  and  $\alpha_2(t)$  are the time-dependent coefficients for each term. Because the vertical  
 191 variation of  $\mathbf{P}$  and  $\mathbf{X}$  are much smaller than the horizontal variation, we can practically ignore the  
 192 vertical component of  $\alpha_1(t)$  and  $\alpha_2(t)$ . Thus,  $\alpha_1(t)$  and  $\alpha_2(t)$  are reduced to a 2-dimensional vector  
 193 to denote the horizontal gradient.

194 Each coefficient can be represented by a linear combination of basis functions  $\Phi_k(t)$ :

$$195 \quad \begin{cases} \alpha_0(t) = \sum_{k=0}^{K_a} a_k^{(0)} \Phi_k^{(0)}(t) \\ \alpha_1(t) = \sum_{k=0}^{K_b} (a_k^{(1E)} \Phi_k^{(1E)}(t), a_k^{(1N)} \Phi_k^{(1N)}(t), 0), \\ \alpha_2(t) = \sum_{k=0}^{K_c} (a_k^{(2E)} \Phi_k^{(2E)}(t), a_k^{(2N)} \Phi_k^{(2N)}(t), 0) \end{cases} \quad (5)$$

196 where  $a_k^{(\cdot)}$  are the coefficients of the  $k$ th basis function,  $\Phi_k^{(\cdot)}(t)$ , for each term named  $\langle \cdot \rangle$ .  $E$  and  $N$  in  
 197  $\langle \cdot \rangle$  denote the eastward and northward components of the vector, respectively. For simplification, we  
 198 compile these coefficients into vector  $\mathbf{a}$ , hereafter.

199 Because the initial values for  $\mathbf{M}$  and  $\mathbf{X}_j$  are usually obtained in the precision of less than meters prior  
 200 to the GNSS-A analysis, we approximate  $\mathbf{P}$  and  $\mathbf{X}_j$  in  $\Gamma$  substituting the initial values, i.e.,  $\mathbf{M}^0$  and  
 201  $\mathbf{X}_j^0$ , and not updating them with the iteration. This reduces the number of estimation parameters in the  
 202 correction term, i.e.,  $\gamma_i = \gamma_i(\mathbf{a} | \mathbf{X}_j^0, \mathbf{M}^0, \mathbf{Q}(t), \boldsymbol{\theta}(t))$ .

## 203 2.4 Rigid array constraints

204 Usually, the local deformation within the transponders' array is assumed to be sufficiently small, so  
 205 that the same array geometry parameters can be used throughout all visits. Because the relative  
 206 positions of the transponders in the array are strongly coupled with the sound speed estimates and the  
 207 position of array centroid, constraining the array geometry is expected to stabilize the GNSS-A  
 208 solutions. Matsumoto et al. (2008) developed the rigid-array constraint, which has been adopted in  
 209 the subsequent studies (e.g., Watanabe et al., 2014; Yokota et al., 2016) except in the cases where the  
 210 rigid-array assumption is inadequate (e.g., Sato et al., 2011).

211 To implement the rigid-array constraint, slight change in the observation equation is needed. We  
 212 divide the transponders' positions as  $\mathbf{X}_j = \overline{\mathbf{X}}_j + \Delta\mathbf{X}$ , where  $\overline{\mathbf{X}}_j$  and  $\Delta\mathbf{X}$  denote the relative positions  
 213 of each transponder and the parallel translation of the transponder array, respectively. The array  
 214 geometry,  $\overline{\mathbf{X}}_j$ , should be determined prior to the analytical procedure, using the data of multiple  
 215 observation visits.

216 Meanwhile,  $\overline{\mathbf{X}}_j$  can also be determined simultaneously with the positioning procedure by combining  
 217 the data vectors, model parameter vectors, and observation equation for all series of the observation  
 218 visits, as the original formulation of Matsumoto et al. (2008). However, it requires huge  
 219 computational resources to solve all the parameters, as the number of observations increases.  
 220 Therefore, we are not concerned with the simultaneous determination of the array geometry in the  
 221 present paper.

## 222 3 Analytical procedures

### 223 3.1 Observation equation

224 In the GNSS-A analysis, observed travel time,  $T_i^o$ , are compared with the model,  $T_i^c$ . For the  
 225 interpretability of variables and the simplification in the expansion, we took the logarithms of travel  
 226 time. Summarizing the above expansion, we put the following observation equation for  $i$ th acoustic  
 227 round-trip travel time:

$$228 \quad \log(T_i^o/T^*) = \log(\tau_i(\mathbf{X}_j, \mathbf{M} | \mathbf{Q}, \boldsymbol{\theta}, V_0)/T^*) - \gamma_i(\mathbf{a} | \mathbf{X}_j^0, \mathbf{M}^0, \mathbf{Q}, \boldsymbol{\theta}) + e_i, \quad (6.1)$$

229 or in the form with the rigid-array constraint,

$$230 \quad \log(T_i^o/T^*) = \log(\tau_i(\Delta \mathbf{X}, \mathbf{M} | \bar{\mathbf{X}}_j, \mathbf{Q}, \boldsymbol{\theta}, V_0)/T^*) - \gamma_i(\mathbf{a} | \mathbf{X}_j^0, \mathbf{M}^0, \mathbf{Q}, \boldsymbol{\theta}) + e_i, \quad (6.2)$$

231 where  $T^*$  is the characteristic travel time and  $e_i$  is the observation error vector. Figure 3 indicates the  
 232 summary for constructing the observation equation. It should be noted that, in this formulation, the  
 233 continuity of sound speed field is assumed.

234 This section shows the algorithm to estimate the model parameters from the nonlinear observation  
 235 equation 6. We took a Bayesian approach because of its simple expression when incorporating prior  
 236 information. Furthermore, it provides a well-defined index for the model selection, i.e., the Akaike's  
 237 Bayesian Information Criterion (ABIC; Akaike, 1980). The expansion shown in this section is based  
 238 on Tarantola and Valette (1982) and Matsu'ura et al. (2007).

### 239 3.2 Prior information

240 The observation equation can be rewritten as,

$$241 \quad \mathbf{y} = \mathbf{f}(\mathbf{x}) + \mathbf{e}, \quad (7)$$

242 where  $\mathbf{x} = [\mathbf{X}_j^T \quad \mathbf{M}^T \quad \mathbf{a}^T]^T$ ,  $y_i = \log(T_i^o/T^*)$ , and  $f_i = \log(\tau_i/T^*) - \gamma_i$ . Let us consider the direct  
 243 prior information for the model parameters  $\mathbf{X}_j$  and  $\mathbf{M}$  written as,

$$244 \quad \begin{bmatrix} \mathbf{X}_j^0 \\ \mathbf{M}^0 \end{bmatrix} = \begin{bmatrix} \mathbf{X}_j \\ \mathbf{M} \end{bmatrix} + \begin{bmatrix} \mathbf{d}_X \\ \mathbf{d}_M \end{bmatrix}, \quad (8)$$

245 where  $\mathbf{X}_j^0$ ,  $\mathbf{M}^0$  and  $\mathbf{d} = [\mathbf{d}_X^T \quad \mathbf{d}_M^T]^T$  denote the predicted model parameter vectors and the error  
 246 vector, respectively. Let us assume that  $\mathbf{d}_X$  and  $\mathbf{d}_M$  follow a normal distribution with a variance-  
 247 covariance of  $D_X(\rho^2)$  and  $D_M(\rho^2)$ , whose scale can be adjusted by a hyperparameter  $\rho^2$ , i.e.,  $D_X =$   
 248  $\rho^2 \widetilde{D}_X$  and  $D_M = \rho^2 \widetilde{D}_M$ , respectively. The prior probability density function (pdf) for the constraints  
 249 can be written as,

$$250 \quad p(\mathbf{X}_j, \mathbf{M}; \rho^2) = c \cdot \exp \left[ -\frac{1}{2} \left( \begin{bmatrix} \mathbf{X}_j^0 \\ \mathbf{M}^0 \end{bmatrix} - \begin{bmatrix} \mathbf{X}_j \\ \mathbf{M} \end{bmatrix} \right)^T \begin{bmatrix} D_X(\rho^2) & 0 \\ 0 & D_M(\rho^2) \end{bmatrix}^{-1} \left( \begin{bmatrix} \mathbf{X}_j^0 \\ \mathbf{M}^0 \end{bmatrix} - \begin{bmatrix} \mathbf{X}_j \\ \mathbf{M} \end{bmatrix} \right) \right], \quad (9)$$

251 where  $c$  denotes the normalization constant.



252 For the model parameter  $\mathbf{a}$ , an indirect prior information can be applied that the temporal change of  
 253 sound speed perturbation model  $\Gamma$  is small. Specifically, the roughness which can be defined by the  
 254 derivatives of each term in equation 4 should be small. In this study, we use the square of second  
 255 derivative as roughness  $\phi$ , whereas Ikuta et al. (2008) used the first derivative. When using the B-  
 256 spline functions  $\Phi_k^{(\cdot)}(t)$  (e.g., de Boor, 1978) as the basis of temporal sound speed variation, the  
 257 roughness can be written in a vector form, i.e.,

$$258 \quad \phi = \int_t \left( \frac{\partial^2 \alpha_{(\cdot)}(t)}{\partial t^2} \right)^2 dt = \mathbf{a}^{(\cdot)T} H_{(\cdot)} \mathbf{a}^{(\cdot)}, \quad (10.1)$$

259 where,

$$260 \quad H_{(\cdot)ij} = \int \frac{\partial^2 \Phi_i^{(\cdot)}(t)}{\partial t^2} \frac{\partial^2 \Phi_j^{(\cdot)}(t)}{\partial t^2} dt. \quad (10.2)$$

261 Then, the prior pdf can be written using the hyperparameter  $\lambda_{(\cdot)}$  as,

$$262 \quad p(\mathbf{a}^{(\cdot)}; \lambda_{(\cdot)}^2) = c \cdot \exp \left[ -\frac{1}{2\lambda_{(\cdot)}^2} \mathbf{a}^{(\cdot)T} H_{(\cdot)} \mathbf{a}^{(\cdot)} \right], \quad (11)$$

263 where  $c$  denotes the normalization constant.

264 Combining these prior informations, we obtain the following prior pdf:

$$265 \quad p(\mathbf{x}; \rho^2, \lambda^2) = (2\pi)^{-\frac{g}{2}} \| \Lambda_G \|^{-\frac{1}{2}} \exp \left[ -\frac{1}{2} (\mathbf{x}^0 - \mathbf{x})^T G(\rho^2, \lambda^2) (\mathbf{x}^0 - \mathbf{x}) \right], \quad (12.1)$$

266 with  $\lambda^2 = [\lambda_0^2 \quad \lambda_{1E}^2 \quad \lambda_{1N}^2 \quad \lambda_{2E}^2 \quad \lambda_{2N}^2]$ ,  $\mathbf{x}^0 = [\mathbf{X}_j^{0T} \quad \mathbf{M}^{0T} \quad \mathbf{0}^T]^T$ , and,

$$267 \quad G(\rho^2, \lambda^2) = \begin{bmatrix} D_X(\rho^2)^{-1} & & & & & & & & & & & \\ & D_M(\rho^2)^{-1} & & & & & & & & & & \\ & & H_0/\lambda_0^2 & & & & & & & & & \\ & & & H_{1E}/\lambda_{1E}^2 & & & & & & & & \\ & & & & H_{1N}/\lambda_{1N}^2 & & & & & & & \\ & & & & & H_{2E}/\lambda_{2E}^2 & & & & & & \\ & & & & & & H_{2N}/\lambda_{2N}^2 & & & & & \end{bmatrix}, \quad (12.2)$$

268 where  $g$  and  $\| \Lambda_G \|$  represent the rank of  $G$  and the absolute value of the product of non-zero  
 269 eigenvalues of  $G$ , respectively.

### 270 3.3 Variance-covariance of data error

271 Now for the observed data, we take the assumption that  $\mathbf{e}$  also follows a normal distribution with a  
 272 variance-covariance of  $\sigma^2 E$ , i.e.,

$$273 \quad p(\mathbf{y}|\mathbf{x}; \sigma^2) = (2\pi\sigma^2)^{-\frac{n}{2}} |E|^{-\frac{1}{2}} \exp \left[ -\frac{1}{2\sigma^2} (\mathbf{y} - \mathbf{f}(\mathbf{x}))^T E^{-1} (\mathbf{y} - \mathbf{f}(\mathbf{x})) \right], \quad (13)$$

274 where  $n$  is the number of data and  $|\cdot|$  denotes the determinant of the matrix.

275 The major error sources for the measurement and calculation of travel time are (1) measurement error  
 276 when reading the return signal, (2) transducer's positioning error, and (3) modeling error of the sound  
 277 speed field. Non-diagonal components of  $E$  are caused not by measurement error, but by transducer's  
 278 positioning error and sound speed modeling error. The transducer's positioning error may have  
 279 temporal correlation which comes from the kinematic GNSS noise. The modeling error has spatio-  
 280 temporal correlation because the sound speed variation is modeled by a smooth function of space and  
 281 time. Thus, we assumed the following covariance terms using two hyperparameters, i.e.,  $\mu_t$  and  $\mu_{MT}$ ,  
 282 to adjust the non-diagonal component of  $E$ :

$$283 \quad E_{ij}(\mu_t, \mu_{MT}) = \begin{cases} \sqrt{E_{ii}E_{jj}} \exp\left(-\frac{|t_i - t_j|}{\mu_t}\right) & \text{if the transponders for } i \text{ and } j \text{ are the same} \\ \mu_{MT} \sqrt{E_{ii}E_{jj}} \exp\left(-\frac{|t_i - t_j|}{\mu_t}\right) & \text{for others} \end{cases}, \quad (14)$$

284 whose formulation refers to Fukahata and Wright (2008). Equation 14 means that the densely  
 285 sampled data would have smaller weights in the model than the isolated data. A factor  $\mu_{MT} \in [0, 1]$   
 286 was introduced to suppress the error correlation between the different transponders because the  
 287 acoustic rays for different transponders take separate paths as the depths increases. Consideration of  
 288 the non-diagonal components of the data variance-covariance contributes to reduce the complexity of  
 289 the model against the excessively high-rate data sampling.

290 Subsequently, we consider the diagonal component of  $E$  which controls the weight of individual data.  
 291 Because the measurement errors of acoustic travel time are caused by mis-reading of the return  
 292 signal, it is independent on the travel time value. Therefore, it is reasonable to put the assumption that  
 293 the error of  $T_i^o - T_i^c$  follows a normal distribution. Nonetheless, because the GNSS-A typically gives  
 294 the precision of  $T_i^o/T_i^c \sim 1 \pm 10^{-4}$ , we can suppose that  $T_i^o/T_i^c$  approximately follows a log-normal  
 295 distribution as assumed in equation 13. In order to put the same weight for all measured travel time in  
 296 the real scale, we applied  $E_{ii} = (T^*/T_i^o)^2$  for scaling the diagonal component.

### 297 3.4 Posterior probability

298 The posterior pdf after the data acquisition, which can be defined to be equal to the likelihood of the  
 299 model parameter with the given data, can be written as,

$$300 \quad p(\mathbf{x}; \sigma^2, \mu_t, \mu_{MT}, \rho^2, \lambda^2 | \mathbf{y}) = c \cdot (2\pi\sigma^2)^{-\frac{(n+g)}{2}} |E|^{-\frac{1}{2}} \|\tilde{\Lambda}_G\|^{\frac{1}{2}} \exp\left[-\frac{1}{2\sigma^2} s(\mathbf{x})\right], \quad (15.1)$$

301 with,

$$302 \quad s(\mathbf{x}) = (\mathbf{y} - \mathbf{f}(\mathbf{x}))^T E^{-1} (\mathbf{y} - \mathbf{f}(\mathbf{x})) + (\mathbf{x}^0 - \mathbf{x})^T \tilde{G} (\mathbf{x}^0 - \mathbf{x}), \quad (15.2)$$

303 where  $\tilde{G} = \sigma^2 G(\rho^2, \lambda^2)$  and  $\|\tilde{\Lambda}_G\|$  represents the absolute value of the product of non-zero  
 304 eigenvalues of  $\tilde{G}$ .

305 Defining  $\hat{\mathbf{x}}(\sigma^2, \mu_t, \mu_{MT}, \rho^2, \lambda^2)$  as  $\mathbf{x}$  that maximizes the posterior probability (equation 15) under the  
 306 given hyperparameters, the partial derivative of  $p(\mathbf{x}|\mathbf{y})$  with respect to  $\mathbf{x}$  should be zero for  $\mathbf{x} = \hat{\mathbf{x}}$ .  
 307 Hence,  $\hat{\mathbf{x}}$  should satisfy the following equation:

$$308 \quad A(\hat{\mathbf{x}})^T E^{-1}(\mathbf{y} - \mathbf{f}(\hat{\mathbf{x}})) + \tilde{G}(\mathbf{x}^0 - \hat{\mathbf{x}}) = \mathbf{0}, \quad (16.1)$$

309 where  $A(\mathbf{x})$  is the Jacobian matrix at point  $\mathbf{x}$  defined as,

$$310 \quad A(\mathbf{x}) = \begin{bmatrix} \frac{\partial f_1}{\partial x_{k1}}(\mathbf{x}) & \cdots & \frac{\partial f_1}{\partial x_{km}}(\mathbf{x}) \\ \vdots & \ddots & \vdots \\ \frac{\partial f_n}{\partial x_{k1}}(\mathbf{x}) & \cdots & \frac{\partial f_n}{\partial x_{km}}(\mathbf{x}) \end{bmatrix}. \quad (16.2)$$

311 We can solve the nonlinear equation 16 numerically by performing an iterative method, where  $\mathbf{x}_k$  is  
 312 corrected in each step with the following algorithm:

$$313 \quad \mathbf{x}_{k+1} = \mathbf{x}_k + (A(\mathbf{x}_k)^T E^{-1} A(\mathbf{x}_k) + \tilde{G})^{-1} (A(\mathbf{x}_k)^T E^{-1} (\mathbf{Y} - \mathbf{f}(\mathbf{x}_k)) + \tilde{G}(\mathbf{x}^0 - \mathbf{x}_k)), \quad (17)$$

314 to satisfy the following convergence criteria:

$$315 \quad A(\mathbf{x}_k)^T E^{-1} (\mathbf{Y} - \mathbf{f}(\mathbf{x}_k)) + \tilde{G}(\mathbf{x}^0 - \mathbf{x}_k) \ll 1. \quad (18)$$

316 Ignoring the term  $O((\mathbf{x} - \hat{\mathbf{x}})^2)$  in  $f(\mathbf{x})$  around  $\hat{\mathbf{x}}$ ,  $s(\mathbf{x})$  can be rewritten as,

$$317 \quad s(\mathbf{x}) \sim s(\hat{\mathbf{x}}) + (\mathbf{x} - \hat{\mathbf{x}})^T (A(\hat{\mathbf{x}})^T E^{-1} A(\hat{\mathbf{x}}) + \tilde{G})(\mathbf{x} - \hat{\mathbf{x}}). \quad (19)$$

318 Therefore, the linearized variance-covariance matrix around  $\hat{\mathbf{x}}$  can be obtained as,

$$319 \quad \hat{C} = \sigma^2 (A(\hat{\mathbf{x}})^T E^{-1} A(\hat{\mathbf{x}}) + \tilde{G})^{-1}. \quad (20)$$

### 320 3.5 Hyperparameter tuning

321 The appropriate values of the hyperparameters can be determined by minimizing Akaike's Bayesian  
 322 Information Criteria (ABIC; Akaike, 1980),

$$323 \quad \text{ABIC} = -2 \log \int p(\mathbf{y}|\mathbf{x}; \sigma^2, \mu_t, \mu_{MT}) p(\mathbf{x}; \rho^2, \lambda^2) d\mathbf{x} + 2N_{\text{HP}}, \quad (21)$$

324 where  $N_{\text{HP}}$  denotes the number of hyperparameters. Although it is difficult to analytically calculate  
 325 the integral for the marginal likelihood because of the nonlinearity in  $\mathbf{f}(\mathbf{x})$ , the Laplace's method can  
 326 be applied in this case where the degree of freedom is sufficiently large and  $s(\mathbf{x})$  can be almost  
 327 unimodal. Thus, an approximated form for ABIC is obtained as follows:

$$328 \quad \text{ABIC} \cong (n + g - m) \log s(\hat{\mathbf{x}}) - \log|E^{-1}| - \log\|\Lambda_G\| + \log|A(\hat{\mathbf{x}})^T E^{-1} A(\hat{\mathbf{x}}) + \tilde{G}| + \text{const}. \quad (22)$$

329 where  $m$  is the number of model parameters. For the derivation, we used the following relationship:

$$330 \quad \sigma^2 = \frac{s(\hat{\mathbf{x}})}{n + g - m}, \quad (23)$$

331 which is derived from the condition that the partial derivative of ABIC with respect to  $\sigma^2$  should be  
 332 zero. We can tune the hyperparameters to minimize the approximated ABIC value defined in  
 333 equation 22, to obtain the solution  $\mathbf{x}^* = \hat{\mathbf{x}}(\sigma^{2*}, \mu_t^*, \mu_{MT}^*, \rho^{2*}, \lambda^{2*})$ , where  $*$  denotes the selected  
 334 hyperparameters.

#### 335 4 Features of “GARPOS”

336 GARPOS (Watanabe et al., 2020a; available at <https://doi.org/10.5281/zenodo.3992688>) has been  
 337 developed to implement the GNSS-A analysis procedure. GARPOS is compatible with Python 3,  
 338 with other packages NumPy, SciPy, pandas, and matplotlib. These packages are pre-installed in most  
 339 of the Python distributions such as Anaconda. Sample scripts and data for testing GARPOS are also  
 340 stored in the repository.

341 GARPOS is distributed as a series of files, which requires a driver script to run. The toolset consists  
 342 of multiple Python files and a Fortran90 library for ray tracing. GARPOS requires the following  
 343 input files:

344 (I-1) Initial site parameter file (in Python’s configuration format),

345 (I-2) Acoustic observation data file (in csv format),

346 (I-3) Reference sound speed data file (in csv format),

347 (I-4) Setting file (in Python’s configuration format).

348 Initial site parameter file (I-1) contains the initial values of the transponders’ positions, the ATD  
 349 offset and the relevant prior covariance information, as well as the metadata for the observation site  
 350 and conditions. Acoustic observation data file (I-2) contains the list of the observation data associated  
 351 with each acoustic ranging, such as travel time, positions, attitude and other metadata. Reference  
 352 sound speed data file (I-3) contains the reference sound speed profile approximated into a polygonal  
 353 curve. Setting file (I-4) contains the parameters to control the analysis procedures including the hyper  
 354 parameters. Users can put the lists of candidates of hyperparameters in which the best combination  
 355 may be within. The parameters  $nmp0$ ,  $nmp1$ , and  $nmp2$  in the setting file control the number of  
 356 basis functions,  $K_a$ ,  $K_b$ , and  $K_c$  in equation 5.

357 The results are written in the following output files:

358 (O-1) Estimated site parameter files (in Python’s configuration format),

359 (O-2) Modified acoustic observation data file (in csv format),

360 (O-3) Model parameter list file (in csv format),

361 (O-4) Posterior variance-covariance matrix file (in csv format).

362 Estimated site parameter files (O-1) is written in the same format as the file (I-1). Modified acoustic  
 363 observation data file (O-2) contains the calculated travel time data and the coefficients of sound  
 364 speed perturbation model, as well as the original data/metadata set in (I-2). Model parameter list file  
 365 (O-3) and posterior variance-covariance matrix file (O-4) contain the whole estimated model  
 366 parameter vector and its variance-covariance, respectively.

367 Major input/output parameters and hyperparameters for GARPOS are listed in Tables 1 and 2,  
368 respectively.

369 We developed GARPOS to be compatible with both observation configurations. When handling the  
370 GNSS-A data collected in the stationary configurations, we should process data with some  
371 constraints on model parameters. Specifically, (1) upward components of transponders' positions  
372 should be fixed to zero, and (2) spatial gradient components of the sound speed perturbation model  
373 should not be solved, i.e.,  $nmp1 = nmp2 = 0$ , because these parameters cannot be well resolved in  
374 the stationary configuration. Although further parameter tuning may be required for optimization,  
375 users can solve the seafloor position by GARPOS with the stationary data in addition to the move-  
376 around data.

## 377 **5 Applications to the actual data**

### 378 **5.1 Data and settings**

379 In order to verify the proposed analytical procedure, we reanalyzed the GNSS-A data at the sites  
380 named “TOS2” and “MYGI” (Table 3, Figure 4) in 2011-2019. The test sites were selected for  
381 several reasons: (1) whereas TOS2 is expected to move at almost constant rate, MYGI will show the  
382 transient displacement due to the postseismic crustal deformation of the 2011 Tohoku-oki  
383 earthquake; (2) the oceanographic environments are different, i.e., the effect of the Kuroshio current  
384 is dominant at TOS2; but (3) the depths of both sites are almost the same. The observation epochs  
385 used in this study is listed in Supplementary Tables 1 and 2. The datasets used in this study are  
386 available at <https://doi.org/10.5281/zenodo.3993912> (Watanabe et al., 2020b).

387 Acoustic round-trip travel times were measured on the survey vessel using the hull-mounted acoustic  
388 transducer (e.g., Ishikawa et al., 2020). Processing delays in the acoustic devices were subtracted  
389 from the acoustic data beforehand.

390 Solid-earth-tide-free positions of GNSS antenna  $\mathbf{Q}(t)$  were determined at 2 Hz by the open source  
391 software RTKLIB version 2.4.2 (Takasu, 2013) in post-processing kinematic Precise Point  
392 Positioning (PPP) mode, using the precise satellite orbit and the 30-sec satellite clock solutions (final  
393 products) provided by the International GNSS Service (International GNSS Service, a; b), in the  
394 same procedures as Watanabe et al. (2020c). The ATD offset values for each vessel,  $\mathbf{M}$ , were  
395 measured by leveling, distance, and angle surveys before the first GNSS-A observation cruise, to be  
396 used as  $\mathbf{M}^0$ .

397 Along with the acoustic observations, the profiles of temperature and/or conductivity were measured  
398 by CTD, XCTD or XBT probes several times. The reference sound speed profile,  $V_0(u)$ , was  
399 calculated from the observed temperature and salinity profiles using the empirical relationship  
400 proposed by Del Grosso (1974). To save the computational cost for ray tracing, the profile was  
401 approximated into a polygonal curve with several tens of nodes (Figure 5).

402 During a GNSS-A survey, the vessel sails on a pre-determined track over the seafloor transponder  
403 array to collect geometrically balanced acoustic data (e.g., Figure 1). The along-track observation  
404 (called “subset”, hereafter) is repeated several times by reversing the sailing direction in order to  
405 reduce the bias due to the errors in the ATD offset.

406 During an observation cruise, it occasionally took more than a few weeks to collect sufficient  
407 acoustic data at a single site due to weather conditions or other operational restrictions. Even so, we

408 compiled a single dataset per site per cruise for the static seafloor positioning in practice, because the  
 409 positional changes should be too small to detect. We call the collection of a single GNSS-A dataset  
 410 “observation epoch” or “epoch”, hereafter.

411 We set the parameters for the numbers of basis functions,  $K_a$ ,  $K_b$ , and  $K_c$ , in equation 5, as  $nmp0 =$   
 412  $nmp1 = nmp2 = 15$  for both preprocess and main process. Knot intervals of B-spline basis  
 413 functions were approximately 10-20 min. for most epochs.

## 414 5.2 Array geometry determination

415 In order to calculate the proper array geometry  $\overline{\mathbf{X}}_j$  for the rigid-array constraint, we first determined  
 416 the positions of each transponder for all observations. Note that not all transponders are used in each  
 417 observation, for example, because of additional installation of transponders for replacing  
 418 transponders which were decommissioned due to battery outage.  $\overline{\mathbf{X}}_j$  and the positional difference of  
 419 the array center for  $n$ th observation,  $\mathbf{c}^{(n)}$  were calculated by solving the following simultaneous  
 420 equations:

$$421 \begin{cases} \mathbf{X}_j^{(n)} = \delta_j^{(n)} \overline{\mathbf{X}}_j + \delta_j^{(n)} \mathbf{c}^{(n)} & (\text{for } j = 1 \dots J \text{ and } n = 1 \dots N) \\ 0 = \sum_{n=1}^N \mathbf{c}^{(n)} \end{cases}, \quad (24.1)$$

422 with,

$$423 \delta_j^{(n)} = \begin{cases} 1 & \text{if the transponder } j \text{ is used in } n \text{ th observation} \\ 0 & \text{others} \end{cases}, \quad (24.2)$$

424 where  $J$  and  $N$  are the number of transponders and observations, respectively, and  $\mathbf{X}_j^{(n)}$  denotes the  
 425 predetermined transponders’ positions for the  $n$ th observation.

426 The preliminary array-free positioning was also used for the verification of the collected data. We  
 427 eliminated the outliers whose discrepancies from the preliminary solution were larger than the  
 428 arbitrary threshold. We set the threshold to be 5 times as large as the root mean square value (RMS)  
 429 of the travel time residuals.

## 430 5.3 Hyperparameter search

431 In order to get the solution  $\mathbf{x}^*$ , we should determine the appropriate values for the various  
 432 hyperparameters, i.e.,  $\sigma^2$ ,  $\mu_t$ ,  $\mu_{MT}$ ,  $\rho^2$ ,  $\lambda_0^2$ ,  $\lambda_{1E}^2$ ,  $\lambda_{1N}^2$ ,  $\lambda_{2E}^2$ , and  $\lambda_{2N}^2$ . In the scheme of the ABIC  
 433 minimization,  $\sigma^2$  can be determined analytically by equation 23. It is reasonable to assume  $\lambda_{1E}^2 =$   
 434  $\lambda_{1N}^2 = \lambda_{2E}^2 = \lambda_{2N}^2$  because these hyperparameters control the smoothness of the spatial sound  
 435 speed structure. We hereafter use a variable  $\lambda_g^2$  to represent the value of these hyperparameters. For  
 436 the purpose of single positioning,  $\rho$  should be a large number, for example in meter-order. The large  
 437  $\rho$  hardly changes the ABIC value and thus the solution.

438 In order to save the computational resources, we should further reduce the number of  
 439 hyperparameters. We tentatively put  $\mu_{MT} = 0.5$ . For the sound speed variations, we had to assume  
 440 the strong constancy of spatial sound speed structure to resolve them with the single transducer  
 441 GNSS-A. For this reason, we selected the ratio of  $\lambda_0^2$  and  $\lambda_g^2$ , as  $\lambda_g^2 = 0.1 \lambda_0^2$ . The last two

442 hyperparameters,  $\mu_t$  and  $\lambda_0^2$ , were determined with the grid search method. The tested values for  $\mu_t$   
 443 and  $\lambda_0^2$  are  $\mu_t = (0 \text{ min.}, 0.5 \text{ min.}, 1 \text{ min.}, 2 \text{ min.}, 3 \text{ min.})$  and  $\lambda_0^2 =$   
 444  $(10^{-3}, 10^{-2}, 10^{-1}, 10^0, 10^1, 10^2)$ , respectively.

## 445 5.4 Results

446 Figure 6 shows the time series of the estimated positions at sites TOS2 and MYGI. The positions are  
 447 aligned to the ITRF 2014 (Altamimi et al., 2016) and transformed into local ENU coordinates.  
 448 Comparing the time series derived by the existing scheme (SGOBS version 4.0.2; used in Yokota et  
 449 al., 2019), GARPOS reproduced almost the same trends for both sites. GARPOS might have  
 450 succeeded in slightly suppressing the dispersion around the averaged velocity extracted from the  
 451 neighboring epochs. Whereas the previous method corrected the sound speed gradient structure with  
 452 step-by-step procedure, the proposed method has an advantage in directly extracting the structure by  
 453 simultaneous estimation of all parameters.

454 TOS2 is located offshore in the south of Shikoku Island, southwestern Japan, above the source region  
 455 of the 1946 Nankaido earthquake (e.g., Sagiya and Thatcher, 1999) along the Nankai Trough.  
 456 According to Yokota and Ishikawa (2020), who investigated the transient deformations at the GNSS-  
 457 A sites along the Nankai Trough, no significant signal was detected at TOS2. The results by the  
 458 proposed method show the same trends as the conventional results. Although the trend of horizontal  
 459 displacement seems to be changed in 2018 or 2019, careful inspection is needed because the  
 460 transponders had been replaced during this period.

461 MYGI is located in the offshore east of Miyagi Prefecture, northeastern Japan, which experienced the  
 462 2011 Tohoku-oki earthquake (Sato et al., 2011). After the earthquake, significant westward  
 463 postseismic movement and subsidence due to the viscoelastic relaxation has been observed at MYGI  
 464 (Watanabe et al., 2014). The postseismic movements continue but appear to decay. It is true that the  
 465 changes in the displacement rate at these sites are crucial in seismic and geodetic researches, but  
 466 discussing these matters is beyond the scope of the present paper. The point is that the seafloor  
 467 positioning results were well reproduced by the proposed method.

## 468 6 Discussions

### 469 6.1 Interpretations for the correction coefficient

470 As mentioned in Section 2.3, it is convenient to relate the correction coefficient to the sound speed  
 471 perturbation by assuming the case for  $|\gamma_i| \ll 1$  for better understanding, though observation equation  
 472 6 is valid for arbitrary value of  $\gamma_i$ . For the relationship  $\delta V_i \sim \gamma_i \bar{V}_0$ , we can convert each term of  $\Gamma$  into  
 473 the dimension of speed and speed gradient as,  $\delta V_0(t) \equiv \bar{V}_0 \alpha_0(t)$ ,  $\mathbf{g}_1(t) \equiv \bar{V}_0 \alpha_1(t)$ , and  $\mathbf{g}_2(t) \equiv$   
 474  $\bar{V}_0 \alpha_2(t)$ .

475 The early models by Fujita et al. (2006) and Ikuta et al. (2008) took only the term  $\delta V_0(t)$  into  
 476 account. Whereas Ikuta et al. (2008) used the cubic B-spline functions as basis functions, Fujita et al.  
 477 (2006) applied the multiple 2nd degree polynomial functions with 10-20-minute time windows.  
 478 Although these models do not include any transponder dependent term  $\mathbf{g}_2(t)$ , the transponder  
 479 independent spatial gradient  $\mathbf{g}_1(t)$  can be indirectly extracted as shown by Yokota et al. (2019).

480 In addition to estimating the term identical to  $\delta V_0$ , Yokota et al. (2019) implemented the additional  
 481 process to estimate  $\mathbf{g}_2$  from the residuals of the solution by the method of Fujita et al. (2006).  
 482 Strictly, the derived parameters in their scheme, i.e.,  $\Delta V_1$  and  $\Delta V_2$  in Yokota et al. (2019), are the

483 same as  $g_1 + g_2$  and  $g_2$  in this study, respectively. For these parameters, our team have already  
 484 made a qualitative interpretation in Yokota and Ishikawa (2019).

485 In order to show the relationship with other conventional models, we expand the proposed  
 486 formulation to those by Honsho et al. (2019), Yasuda et al. (2017) and Kinugasa et al. (2020).  
 487 Because Honsho et al. (2019) practically assumed 1-directional sound speed gradient, they  
 488 constructed the model basically in the 2-dimensional plane spanned by the gradient direction and  
 489 vertical direction.

490 For simplification, we assume that the ray path is a straight line connecting both ends. Putting  $L^*$   
 491 equal to the depth of the observation site, the emission angle  $\theta$  defined in Figure 3 of Honsho et al.  
 492 (2019) can be expressed as,

$$493 \quad \frac{X_j}{L^*} - \frac{P(t)}{L^*} = \tan \theta. \quad (25)$$

494 Furthermore, assuming that the transmit/reception positions are the same and that the difference  
 495 between transmit/reception time is so small that  $\alpha_0(t)$ ,  $\alpha_1(t)$  and  $\alpha_2(t)$  hardly change,  $\gamma_i$  can be  
 496 written as,

$$497 \quad \gamma_i = \alpha_0(t) + (\alpha_1(t) + \alpha_2(t)) \frac{P(t)}{L^*} + \alpha_2(t) \tan \theta. \quad (26)$$

498 Because  $\delta T$  defined in equations 2 and 5 of Honsho et al. (2019) is equivalent to  $T_i^c - \tau_i$  in our  
 499 formulation, we have,

$$500 \quad (\exp(-\gamma_i) - 1)\tau_i = \frac{1}{\cos \theta} (c_0(t) + g(t)x_0 + w(t) \tan \theta), \quad (27)$$

501 where  $c_0(t)$ ,  $g(t)$ ,  $w(t)$  and  $x_0 = P$  are defined in equations 6, 7, 8 of Honsho et al. (2019) and the  
 502 transducer's position in their formulation, respectively. Recalling that the slant range of acoustic ray  
 503 path is  $2L^* / \cos \theta$ , the reference round-trip travel time can be written as,

$$504 \quad \tau_i = \frac{2L^*}{V_0(u) \cos \theta}. \quad (28)$$

505 Considering the case where  $|\gamma_i| \ll 1$ , equation 27 is approximated to,

$$506 \quad -\frac{2L^*}{V_0} \gamma_i = c_0(t) + g(t)x_0 + w(t) \tan \theta. \quad (29)$$

507 From equations 26 and 29, the following relationships are derived:

$$508 \quad c_0(t) = -\frac{2L^*}{V_0} \alpha_0(t), \quad (30.1)$$

$$509 \quad g(t) = -\frac{2}{V_0} (\alpha_1(t) + \alpha_2(t)), \quad (30.2)$$



510 
$$w(t) = -\frac{2L^*}{\bar{V}_0} \alpha_2(t). \quad (30.3)$$

511 In Honscho et al. (2019),  $w(t)$  is extended to a 2-dimensional vector, i.e.,

512 
$$\mathbf{w}(t) = -\frac{2L^*}{\bar{V}_0} \boldsymbol{\alpha}_2(t). \quad (31.1)$$

513 Similarly, when extending  $g(t)$  to the 2-dimensional vector, we can use the following vector form:

514 
$$\mathbf{g}(t) = -\frac{2}{\bar{V}_0} (\boldsymbol{\alpha}_1(t) + \boldsymbol{\alpha}_2(t)), \quad (31.2)$$

515 though they consequently use the assumption that  $\mathbf{g}(t)$  is parallel to  $\mathbf{w}(t)$ . It is equivalent to the case  
516 that  $\boldsymbol{\alpha}_1$  is parallel to  $\boldsymbol{\alpha}_2$  in the proposed formulation.

517 Honscho et al. (2019) supposed the physical model where a spatially homogeneous 1-directional  
518 gradient of slowness lies in the certain layer, from sea-surface to the depth  $D$ , in the water. In such  
519 cases,  $\mathbf{w}(t)$  is proportional to  $\mathbf{g}(t)$ , as  $\mathbf{w} = (D/2)\mathbf{g}$ . This is exactly the same assumption as the  
520 model by Yasuda et al. (2017). The model of Kinugasa et al. (2020) is the special case of those  
521 models where  $D$  equals to the water depth.

522 In the proposed method, the sound speed field is approximately interpreted by their models when the  
523 unit vector of  $\boldsymbol{\alpha}_1$  is supposed to be same as that of  $\boldsymbol{\alpha}_2$  and  $|\boldsymbol{\alpha}_1| \geq |\boldsymbol{\alpha}_2|$ . The depth of the gradient  
524 layer is calculated as,

525 
$$D = \frac{2L^*}{1 + \boldsymbol{\alpha}_1/\boldsymbol{\alpha}_2}. \quad (32)$$

526 When  $\boldsymbol{\alpha}_1 = \boldsymbol{\alpha}_2$ , it concludes to the model of Kinugasa et al. (2020). Conversely, when  $|\boldsymbol{\alpha}_2| \ll |\boldsymbol{\alpha}_1|$ ,  
527 sound speed gradient lies in the thin layer near the surface.

528 In addition to the simple model above, the proposed method can extract more complicated sound  
529 speed field, which partly described by Yokota and Ishikawa (2019). Extracted parameters for the  
530 sound speed perturbation indicate the complicity of oceanographic structure, as shown in the next  
531 section.

## 532 6.2 Validity of extracted sound speed perturbation model

533 Typical examples for the estimation results for each observation, i.e., the time series of travel time  
534 residuals, and sound speed perturbation interpreted from the correction coefficient, are shown in  
535 Figure 7. Results for all the datasets are available in Supplementary Figure 1.

536 In the most cases for site TOS2, both terms of the estimated sound speed gradient vector stably direct  
537 south to southeast. Because the sound speed increase with the water temperature, it means that the  
538 water temperature is higher in the southern region. The results that  $\mathbf{g}_2$  is comparable with  $\mathbf{g}_1$  in many  
539 cases indicate that the gradient of water temperature continues to the deeper portion, as discussed in  
540 the previous section. This is consistent with the fact that the Kuroshio current continuously flows on  
541 the south of TOS2.

542 In contrast, the directions of gradient terms at MYGI have less constancy than TOS2. Unlike the area  
 543 around TOS2 where the Kuroshio current dominantly affects the seawater structure, MYGI is located  
 544 in an area with a complicated ocean current system (e.g., Yasuda, 2003; Miyazawa et al., 2009).  
 545 Watanabe and Uchida (2016) have also shown that the temperature profiles at MYGI vary widely  
 546 with observation epochs. These features cannot be resolved by the simpler model with single sound  
 547 speed gradient parameter.

548 The complexity in the sound speed variation at MYGI tends to lead to large variations in the residual  
 549 travel time. Nevertheless, the proposed method successfully extracted the smooth sound speed  
 550 structure for many observation epochs, except a few epochs such as June 2013  
 551 (MYGI.1306.kaiyo\_k4) and June 2019 (MYGI.1906.meiyo\_m5) shown in Supplementary Figure 1.  
 552 In these epochs, relatively larger values for the hyperparameter  $\lambda_0^2$  were adopted and caused larger  
 553 variations in each term of  $\Gamma$ . Possible causes of this include the systematic errors in other observation  
 554 subcomponents such as the random walk noise in GNSS positioning, the drifts of gyro sensor, or the  
 555 time synchronization error between the devices.

556 Preferred models for all the tested epochs had positive values for data correlation length,  $\mu_t$ . It is  
 557 considered that the plausible estimation of sound speed is realized by introducing the statistic  
 558 information criteria and the information of data covariances.

559 In order to discuss the effects of the data covariance, we tested the cases for the models without  
 560 assuming the data correlation, i.e.,  $\mu_t = 0$ . Figure 8 shows the preferred models selected from  $\lambda_0^2 =$   
 561  $(10^{-3}, 10^{-2}, 10^{-1}, 10^0, 10^1, 10^2, 10^3, 10^4)$  and  $\mu_t = 0$ . It is clear that the preferred models without  
 562 assuming the data correlation have larger  $\lambda_0^2$ . Although the residuals of travel time were reduced in  
 563 these models, overfittings occurred for each term of  $\Gamma$ . Comparing the preferred and less-preferred  
 564 results, the existence of data covariance components contributes to suppressing the overfitting and to  
 565 selecting a model with less perturbation by decreasing the impact of individual data on model  
 566 parameters.

567 To confirm the stability of the seafloor positioning results, the differences of seafloor position for the  
 568 tested models from the most preferred models are summarized in Figure 9. The differences in  
 569 estimated positions for most of the tested models converged in several centimeters. For both sites,  
 570 variations in the vertical component tend to be larger for larger values of  $\lambda_0^2$ . It indicates that finer  
 571 hyperparameter tuning is not required when considering the application to seafloor positioning.

572 As another application of GNSS-A to oceanography, temporal changes of the oceanographic  
 573 structure within the observation epoch can be extracted using the proposed method. For example, the  
 574 estimated sound speed gradient  $\mathbf{g}_1$  in the epoch of MYGI.1802.kaiyo\_k4 (Figure 7f) suggests that the  
 575 dominant oceanographic structure had changed at 01:00-03:00 UTC. On the other hand, a temporal  
 576 variation with a relatively short period of several tens of minutes remains in the travel time residuals,  
 577 which might be caused by the internal gravity wave. To improve the detectability of relatively short-  
 578 period perturbations, further adjustments and verifications of the proposed model will be required.

## 579 7 Conclusions

580 We reconstructed the GNSS-A observation equation and developed the Python-based software  
 581 GARPOS to solve the seafloor position as well as the sound speed perturbations using the empirical  
 582 Bayes approach. It provides a stable solution for a generally ill-posed problem caused by the

583 correlation among the model parameters, by introducing the hyperparameter tuning based on the  
584 ABIC minimization and data covariance to rationalize the normalization constant of the posterior pdf.

585 The most important point is that the proposed method succeeded in directly extracting the time-  
586 dependent sound speed field with two end members of spatial gradient terms, which are roughly  
587 characterized by depths, even when the observers used only one sea-surface unit. Statistical approach  
588 allowed us to suppress the overfitting and thus to obtain simpler sound speed field from densely  
589 collected dataset. It successfully reproduced the stationary southward sound speed gradient at TOS2,  
590 which is consistent with the Kuroshio current.

591 On the other hand, model overfits were shown in several epochs. These overfits can be caused not  
592 only by the actually complicated sound speed field but also by other error sources which were not  
593 well included in the model. It means that the hyperparameter tuning also plays a role in the  
594 verification of dataset and model. Error analyses in such cases might rather help improving the  
595 GNSS-A accuracy and methodology.

596 We suggested a simplified formatting for the GARPOS input files. Researchers can enter into the  
597 field of seafloor geodesy by collecting the listed data with adequate precision. Since each  
598 subcomponent of GNSS-A technique, i.e., GNSS positioning, acoustic ranging, and so on, has been  
599 well established, observers can combine them on their platform. Especially, GNSS-A is expected to  
600 be practicalized in the near future with an unmanned surface vehicle (Chadwell, 2016) or a buoy  
601 (e.g., Tadokoro et al., 2020; Kinugasa et al., 2020). Even in the case of the stationary observation due  
602 to small cruising speed, GARPOS may provide the solutions by making a slight modification in the  
603 prior variance-covariance matrix.

604 There is a room for improvement in setting the prior information for transponders' positions,  $\mathbf{X}_j^0$ . For  
605 instance, the displacement of transponder array from the previous epoch is predicted as small as  
606 several centimeters when the interval of observation visits is short. Such assumption leads to the  
607 application of the inter-epoch filtering. Furthermore, it has a possibility to progress to the kinematic  
608 seafloor positioning, as shown by Tomita et al. (2019). We expect that the publication of GARPOS  
609 on the open-access repository will enhance the researchers' engagement and the future development  
610 on the GNSS-A technique.

## 611 **8 Conflict of Interest**

612 The authors declare no conflict of interest.

## 613 **9 Data Availability**

614 The datasets analyzed in this study can be found in an open access repository at  
615 <https://doi.org/10.5281/zenodo.3993912> (Watanabe et al., 2020b). The code developed in this study  
616 is available at <http://doi.org/10.5281/zenodo.3992688> (Watanabe et al., 2020a)

## 617 **10 Author Contributions**

618 SW designed the study and wrote the manuscript. SW developed “GARPOS” and processed the data.  
619 SW, TI, YY, and YN discussed about the methodology and commented to improving the manuscript.

## 620 **11 Funding**

621 The submission of the manuscript was funded by the Japan Coast Guard.

## 622 12 Abbreviations

623 ABIC, Akaike Bayesian Information Criterion; ATD offset, Antenna – Transducer offset; GNSS,  
624 Global Navigation Satellite System; GNSS-A, Global Navigation Satellite System – Acoustic  
625 Ranging combined technique; pdf, probability density function.

## 626 13 Acknowledgments

627 We thank many staff members from the Hydrographic and Oceanographic Department, Japan Coast  
628 Guard, including the crew of the survey vessels Takuyo, Shoyo, Meiyo, and Kaiyo for their support  
629 in our observations and technological developments. We especially thank the active senior staff  
630 members from the Geodesy and Geophysics Office, Hydrographic and Oceanographic Department,  
631 Japan Coast Guard, for their devoted maintenance and management of the equipment. We also thank  
632 the reviewers for their comments and suggestions for improving the manuscript.

## 633 14 References

- 634 Akaike, H. (1980). Likelihood and the Bayes procedure. In J. M. Bernardo, et al. (Eds.), *Bayesian*  
635 *Statistics* (pp. 143–166). Valencia, Spain: University Press.
- 636 Altamimi, Z., P. Rebischung, L. Métivier, and C. Xavier (2016). ITRF2014: A new release of the  
637 International Terrestrial Reference Frame modeling nonlinear station motions, *J. Geophys. Res.*  
638 *Solid Earth*, 121. doi:10.1002/2016JB013098
- 639 Asada, A., and Yabuki, T. (2001). Centimeter-level positioning on the seafloor. *Proc. Jpn Acad. Ser.*  
640 *B* 77, 7–12. doi:10.2183/pjab.77.7
- 641 De Boor, C. (1978), *A Practical Guide to Splines*, Vol. 27, Springer-Verlag New York.
- 642 Bürgmann, R., and Chadwell, C. D. (2014). Seafloor geodesy. *Ann. Rev. Earth Planet. Sci.*, 42(1),  
643 509–534. doi:10.1146/annurev-earth-060313-054953
- 644 Chadwell, C. D., and Spiess, F. N. (2008). Plate motion at the ridge-transform boundary of the south  
645 Cleft segment of the Juan de Fuca Ridge from GPS-Acoustic data. *J. Geophys. Res.*, 113,  
646 B04415, doi:10.1029/2007JB004936
- 647 Chadwell, C. D., and Sweeney, A. D. (2010). Acoustic ray-trace equations for seafloor geodesy.  
648 *Marine Geodesy* 33(2–3):164–186. doi:10.1080/01490419.2010.492283
- 649 Chadwell, C. D. (2016). Campaign-style GPS-Acoustic with wave gliders and permanent seafloor  
650 benchmarks, in *Proceedings of the Subduction Zone Observatory Workshop*, Boise Center,  
651 Boise, ID, Sep. 29 – Oct. 1 2016, Boise, ID.
- 652 Chen, H.-Y., Ikuta, R., Lin, C.-H., Hsu, Y.-J., Kohmi, T., Wang, C.-C., Yu, S.-B., Tu, Y., Tsujii, T.,  
653 and Ando, M. (2018), Back-arc opening in the western end of the Okinawa Trough revealed  
654 from GNSS/Acoustic Measurements. *Geophys. Res. Lett.*, 45, 137– 145,  
655 doi:10.1002/2017GL075724

- 656 Fujimoto, H. (2014), Seafloor geodetic approaches to subduction thrust earthquakes, *Monogr.*  
 657 *Environ. Earth Planets*, 2, 23–63, doi:10.5047/meep.2014.00202.0023
- 658 Fujita, M., Ishikawa, T., Mochizuki, M., Sato, M., Toyama, S., Katayama, M., Kawai, K.,  
 659 Matsumoto, Y., Yabuki, T., Asada, A. and Colombo, O. L. (2006). GPS/acoustic seafloor  
 660 geodetic observation: method of data analysis and its application. *Earth Planet. Space*, 58, 265–  
 661 275. doi:10.1186/BF03351923
- 662 Fukahata, Y. and Wright, T. J., (2008). A non-linear geodetic data inversion using ABIC for slip  
 663 distribution of a fault with an unknown dip angle, *Geophys. J. Int.*, 173, 353–364,  
 664 doi:10.1111/j.1365-246X.2007.03713.x
- 665 Gagnon, K., Chadwell, C. D., and Norabuena, E. (2005). Measuring the onset of locking in the Peru-  
 666 Chile trench with GPS and acoustic measurements. *Nature*, 434(7030), 205–208.,  
 667 doi:10.1038/nature03412
- 668 Del Grosso, V. A. (1974), New equation for the speed of sound in natural waters (with comparisons  
 669 to other equations), *J. Acoust. Soc. Am.*, 56, 1084-1091. doi;10.1121/1.1903388
- 670 Honsho, C., and Kido, M. (2017). Comprehensive analysis of traveltime data collected through GPS-  
 671 acoustic observation of seafloor crustal movements. *J. Geophys. Res. Solid Earth*, 122, 8583–  
 672 8599, doi:10.1002/2017JB014733
- 673 Honsho, C., Kido, M., Tomita, F., and Uchida, N. (2019). Offshore postseismic deformation of the  
 674 2011 Tohoku earthquake revisited: Application of an improved GPS-acoustic positioning  
 675 method considering horizontal gradient of sound speed structure. *J. Geophys. Res. Solid Earth*,  
 676 124, doi:10.1029/2018JB017135
- 677 Hovem, J. M. (2013). *Ray Trace Modeling of Underwater Sound Propagation, Modeling and*  
 678 *Measurement Methods for Acoustic Waves and for Acoustic Microdevices*, Marco G. Beghi,  
 679 IntechOpen, doi:10.5772/55935
- 680 IERS Conventions (2010). Gérard Petit and Brian Luzum (eds.). (IERS Technical Note; 36)  
 681 Frankfurt am Main: Verlag des Bundesamts für Kartographie und Geodäsie, 2010. 179 pp.,  
 682 ISBN 3-89888-989-6
- 683 Ikuta, R., Tadokoro, K., Ando, M., Okuda, T., Sugimoto, S., Takatani, K., Yada, K., and Besana, G.  
 684 M. (2008). A new GPS-acoustic method for measuring ocean floor crustal deformation:  
 685 Application to the Nankai Trough. *J. Geophys. Res.*, 113, B02401. doi:10.1029/2006JB004875
- 686 International GNSS Service (a). GNSS Final Combined Orbit Solution Product, Greenbelt, MD,  
 687 USA: NASA Crustal Dynamics Data Information System (CDDIS).  
 688 doi:10.5067/gnss/gnss\_igsorb\_001
- 689 International GNSS Service (b). GNSS Final Combined Satellite and Receiver Clock Solution (30  
 690 second) Product, Greenbelt, MD, USA: NASA Crustal Dynamics Data Information System  
 691 (CDDIS). doi:10.5067/GNSS/gnss\_igsclk30\_001

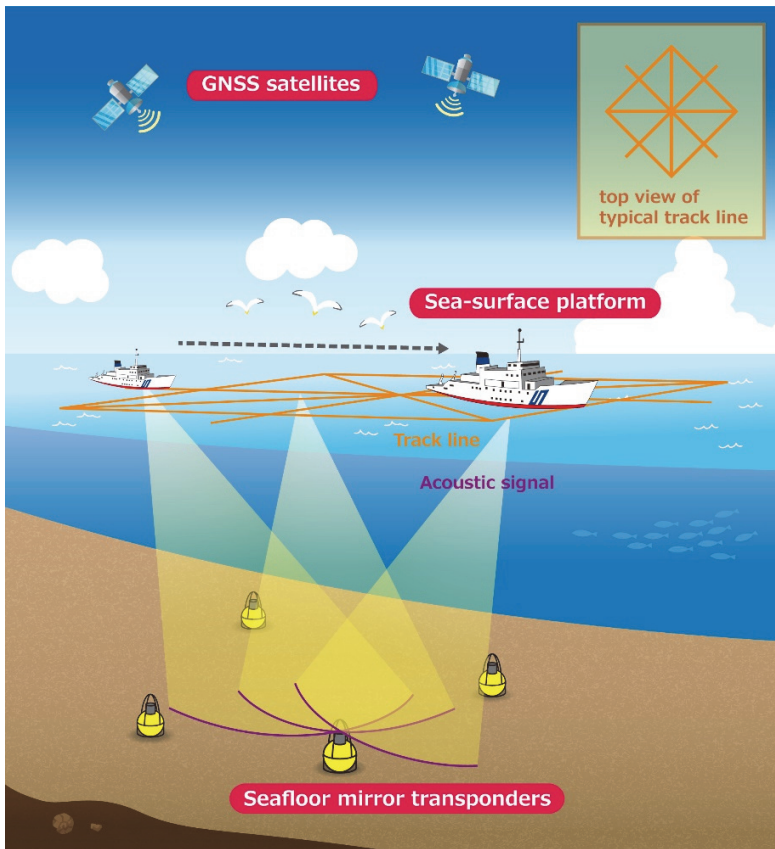
- 692 Ishikawa, T., Yokota, Y., Watanabe, S., and Nakamura, Y. (2020). History of on-board equipment  
693 improvement for GNSS-A observation with focus on observation frequency, *Front. Earth Sci.*,  
694 8:150. doi:10.3389/feart.2020.00150
- 695 Jensen, F. B., Kuperman, W. A., Porter, M. B., and Schmidt, H. 2011. *Computational Ocean*  
696 *Acoustics*, volume 97. New York, NY: Springer New York, ISBN:978-1-4419-8677-1.
- 697 Kido, M., Osada, Y., and Fujimoto, H. (2008). Temporal variation of sound speed in ocean: A  
698 comparison between GPS/acoustic and in situ measurements, *Earth Planet. Space*, 60(3), 229–  
699 234, doi:10.1186/BF03352785.
- 700 Kido, M., Osada, Y., Fujimoto, H., Hino, R., and Ito, Y. (2011). Trench-normal variation in observed  
701 seafloor displacements associated with the 2011 Tohoku-Oki earthquake. *Geophys. Res. Lett.*,  
702 38, L24303. doi:10.1029/2011GL050057
- 703 Kinugasa, N., Tadokoro, K., Kato, T., and Terada, Y. (2020) Estimation of temporal and spatial  
704 variation of sound speed in ocean from GNSS-A measurements for observation using moored  
705 buoy. *Prog. Earth Planet. Sci.*, 7, 21. <https://doi.org/10.1186/s40645-020-00331-5>
- 706 Matsumoto, Y., Fujita, M., and Ishikawa, T. (2008). Development of multi-epoch method for  
707 determining seafloor station position [in Japanese], *Rep. Hydrogr. Oceanogr. Res.*, 26, 16-22
- 708 Matsu'ura, M., Noda, A., and Fukahata, Y. (2007). Geodetic data inversion based on Bayesian  
709 formulation with direct and indirect prior information, *Geophys. J. Int.*, 171(3), 1342–1351.  
710 doi:10.1111/j.1365-246X.2007.03578.x
- 711 Miyazawa, Y., Zhang, R., Guo, X., Tamura, H., Ambe, D., Lee, J.-S., Okuno, A., Yoshinari, H.,  
712 Setou, T., and Komatsu, K. (2009) Water mass variability in the western North Pacific detected  
713 in a 15-year eddy resolving ocean reanalysis. *J. Oceanogr.*, 65, 737–756, doi:10.1007/s10872-  
714 009-0063-3
- 715 Nagaya, Y. (1995). Basic study on a sea floor strain measurement using acoustic techniques [in  
716 Japanese with English abstracts], *Rep. Hydro. Res.*, 31, 67–76.
- 717 Obana, K., Katao, H., and Ando, M. (2000) Seafloor positioning system with GPS-acoustic link for  
718 crustal dynamics observation—a preliminary result from experiments in the sea—. *Earth Planet.*  
719 *Space*, 52, 415–423. doi:10.1186/BF03352253
- 720 Osada, Y., Fujimoto, H., Miura, S., Sweeney, A., Kanazawa, T., Nakao, S., Sakai, S., Hildebrand, J.  
721 A., and Chadwell, C. D. (2003), Estimation and correction for the effect of sound velocity  
722 variation on GPS/Acoustic seafloor positioning: An experiment off Hawaii Island, *Earth Planet.*  
723 *Space*, 55, e17–e20. doi:10.1186/BF03352464
- 724 Sagiya, T., and Thatcher, W. (1999). Coseismic slip resolution along a plate boundary megathrust:  
725 The Nankai Trough, southwest Japan, *J. Geophys. Res.*, 104(B1), 1111- 1129,  
726 doi:10.1029/98JB02644
- 727 Sakic, P., Ballu, V., Crawford, W. C., and Wöppelmann, G. (2018) Acoustic Ray Tracing  
728 Comparisons in the Context of Geodetic Precise off-shore Positioning Experiments, *Marine*  
729 *Geodesy*, 41:4, 315-330, doi:10.1080/01490419.2018.1438322

- 730 Sato, M., Ishikawa, T., Ujihara, N., Yoshida, S., Fujita, M., Mochizuki, M., and Asada, A. (2011).  
 731 Displacement above the hypocenter of the 2011 Tohoku-oki earthquake. *Science* 332, 1395.  
 732 doi:10.1126/science.1207401
- 733 Sato, M., Fujita, M., Matsumoto, Y., Saito, H., Ishikawa, T., and Asakura, T. (2013a). Improvement  
 734 of GPS/acoustic seafloor positioning precision through controlling the ship's track line. *J. Geod.*,  
 735 118, 1–10. doi:10.1007/s00190-013-0649-9
- 736 Spiess, F. N. (1980). Acoustic techniques for Marine Geodesy, *Marine Geodesy*, 4:1, 13-27,  
 737 doi:10.1080/15210608009379369
- 738 Spiess, F. N., Chadwell, C. D., Hildebrand, J. A., Young, L. E., Purcell, G. H. Jr., and Dragert, H.  
 739 (1998). Precise GPS/acoustic positioning of seafloor reference points for tectonic studies. *Phys.*  
 740 *Earth Planet. Inter.*, 108(2), 101–112, doi:10.1016/S00319201(98)00089-2
- 741 Tadokoro K, Kinugasa N, Kato T, Terada Y and Matsuhiro K (2020) A marine-buoy-mounted  
 742 system for continuous and real-time measurement of seafloor crustal deformation. *Front. Earth*  
 743 *Sci.* 8:123. doi: 10.3389/feart.2020.00123
- 744 Takasu, T. (2013), RTKLIB Ver. 2.4.2: An Open Source Program Package for GNSS Positioning,  
 745 <http://www.rtklib.com/>
- 746 Tarantola, A., and Valette, B. (1982). Generalized nonlinear inverse problems solved using the least  
 747 squares criterion, *Rev. Geophys.*, 20(2), 219-232, doi:10.1029/RG020i002p00219
- 748 Tomita, F., Kido, M., Osada, Y., Hino, R., Ohta, Y., and Iinuma, T. (2015). First measurement of the  
 749 displacement rate of the Pacific Plate near the Japan Trench after the 2011 Tohoku-Oki  
 750 earthquake using GPS/acoustic technique. *Geophys. Res. Lett.*, 42, 8391–8397,  
 751 doi:10.1002/2015GL065746
- 752 Tomita, F., Kido, M., Ohta, Y., Iinuma, T., and Hino, R. (2017). Along-trench variation in seafloor  
 753 displacements after the 2011 Tohoku earthquake. *Sci. Adv.*, 3(7), e1700113,  
 754 doi:10.1126/sciadv.1700113
- 755 Tomita, F., Kido, M., Honsho, C., and Matsui, R. (2019). Development of a kinematic GNSS-  
 756 Acoustic positioning method based on a state-space model. *Earth Planet. Space*, 71, 102.  
 757 doi:10.1186/s40623-019-1082-y
- 758 Watanabe, S., Sato, M., Fujita, M., Ishikawa, T., Yokota, Y., Ujihara, N., and Asada, A. (2014).  
 759 Evidence of viscoelastic deformation following the 2011 Tohoku-oki earthquake revealed from  
 760 seafloor geodetic observation. *Geophys. Res. Lett.* 41:5789-5796. doi:10.1002/2014GL061134
- 761 Watanabe, S., and Uchida, T. (2016). Stable structures of temperature and salinity validated by the  
 762 repeated measurements in the few-miles square regions off Japan coast in the western Pacific [in  
 763 Japanese with English abstract]. *Rep. Hydro. Ocean. Res.*, 53, 57–81.
- 764 Watanabe, S., Ishikawa, T., Yokota, Y., and Nakamura, Y. (2020a). GARPOS v0.1.0: Analysis tool  
 765 for GNSS-Acoustic seafloor positioning (Version 0.1.0). Zenodo. doi:10.5281/zenodo.3992688

- 766 Watanabe, S., Ishikawa, T., Yokota, Y., and Nakamura, Y. (2020b). GNSS-A data obtained at the  
767 sites "TOS2" and "MYGI" in 2011-2019. Zenodo. doi:10.5281/zenodo.3993912
- 768 Watanabe, S., Yokota, Y., and Ishikawa, T. (2020c) Stability Test to Validate the GNSS-A Seafloor  
769 Positioning with Kinematic Precise Point Positioning [in Japanese with English abstract and  
770 captions]. *J. Geod. Soc. Japan*, 66, 1-7, doi:10.11366/sokuchi.66.1
- 771 Yasuda, I. (2003). Hydrographic Structure and Variability in the Kuroshio-Oyashio Transition Area.  
772 *J. Oceanogr.*, 59, 389–402, doi:10.1023/A:1025580313836
- 773 Yasuda, K., Tadokoro, K., Taniguchi, S., Kimura, H., and Matsuhiro, K. (2017). Interplate locking  
774 condition derived from seafloor geodetic observation in the shallowest subduction segment at the  
775 Central Nankai Trough, Japan. *Geophys. Res. Lett.*, 44, 3572–3579, doi:10.1002/2017GL072918
- 776 Yokota, Y., Ishikawa, T., Watanabe, S., Tashiro, T., and Asada, A. (2016) Seafloor geodetic  
777 constraints on interplate coupling of the Nankai Trough megathrust zone. *Nature*, 534, 374–377,  
778 doi:10.1038/nature17632
- 779 Yokota, Y., Ishikawa, T., and Watanabe, S. (2018). Seafloor crustal deformation data along the  
780 subduction zones around Japan obtained by GNSS-A observations. *Sci. Data*, 5, 180182.  
781 doi:10.1038/sdata.2018.182
- 782 Yokota, Y., and Ishikawa, T. (2019). Gradient field of undersea sound speed structure extracted from  
783 the GNSS-A oceanography: GNSS-A as a sensor for detecting sound speed gradient. *SN Appl.*  
784 *Sci.*, 1, 693. doi:10.1007/s42452-019-0699-6
- 785 Yokota, Y., Ishikawa, T., and Watanabe, S. (2019). Gradient field of undersea sound speed structure  
786 extracted from the GNSS-A oceanography. *Mar. Geophys. Res.*, 40(4), 493-504.  
787 doi:10.1007/s11001-018-9362-7
- 788 Yokota, Y. and Ishikawa, T. (2020), Shallow slow slip events along the Nankai Trough detected by  
789 GNSS-A, *Sci. Adv.*, 6(3), eaay5786. doi:10.1126/sciadv.aay5786
- 790

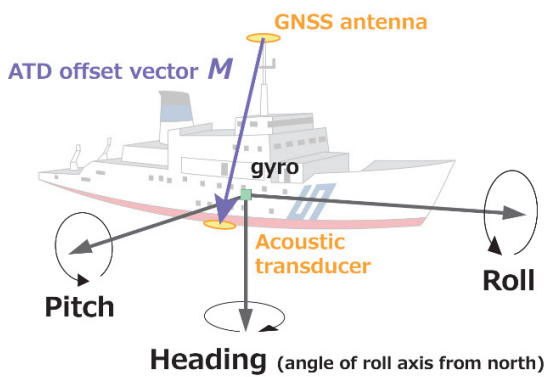


791 15 Figures



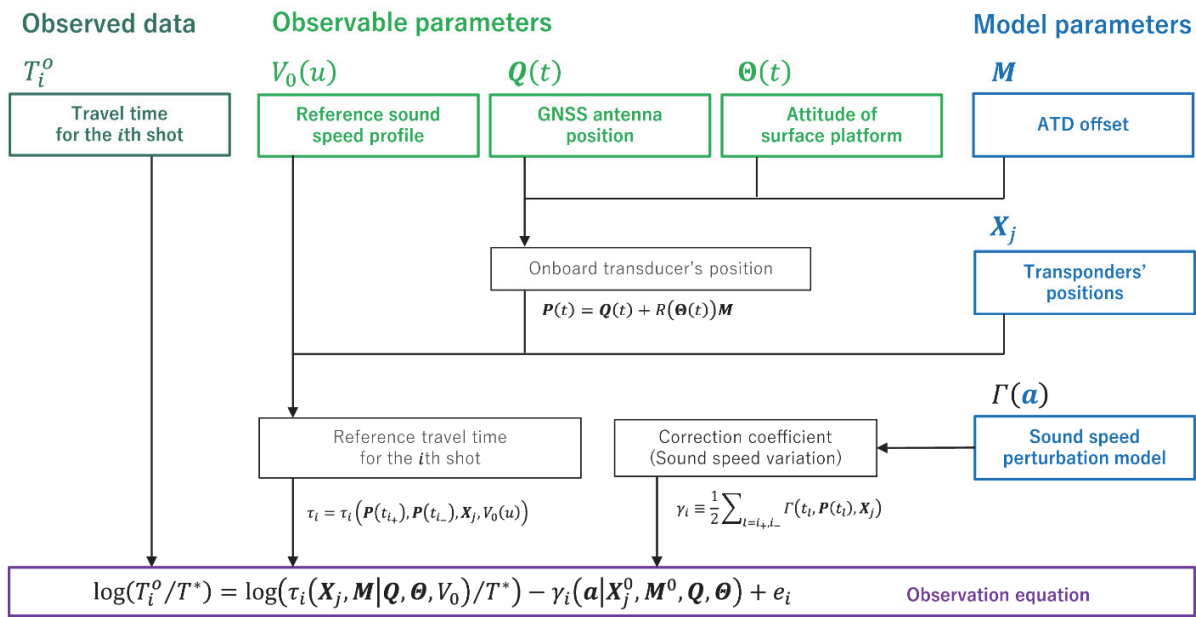
792  
793 Figure 1. Schematic image of the GNSS-A system in the move-around configuration.

794



795  
796 Figure 2. Definitions of the attitude parameters and the ATD offset vector for the sea-surface  
797 platform. Heading is zero when the roll axis directs to the north. The roll and pitch axes direct  
798 forward and rightward (portside) of the vessel, respectively.

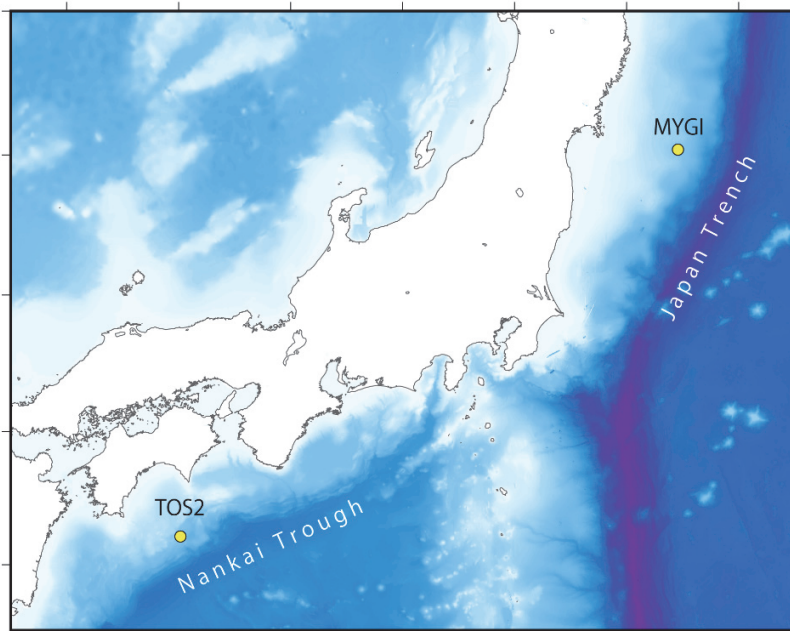
799



800

801 Figure 3. Flow chart to construct the observation equation.

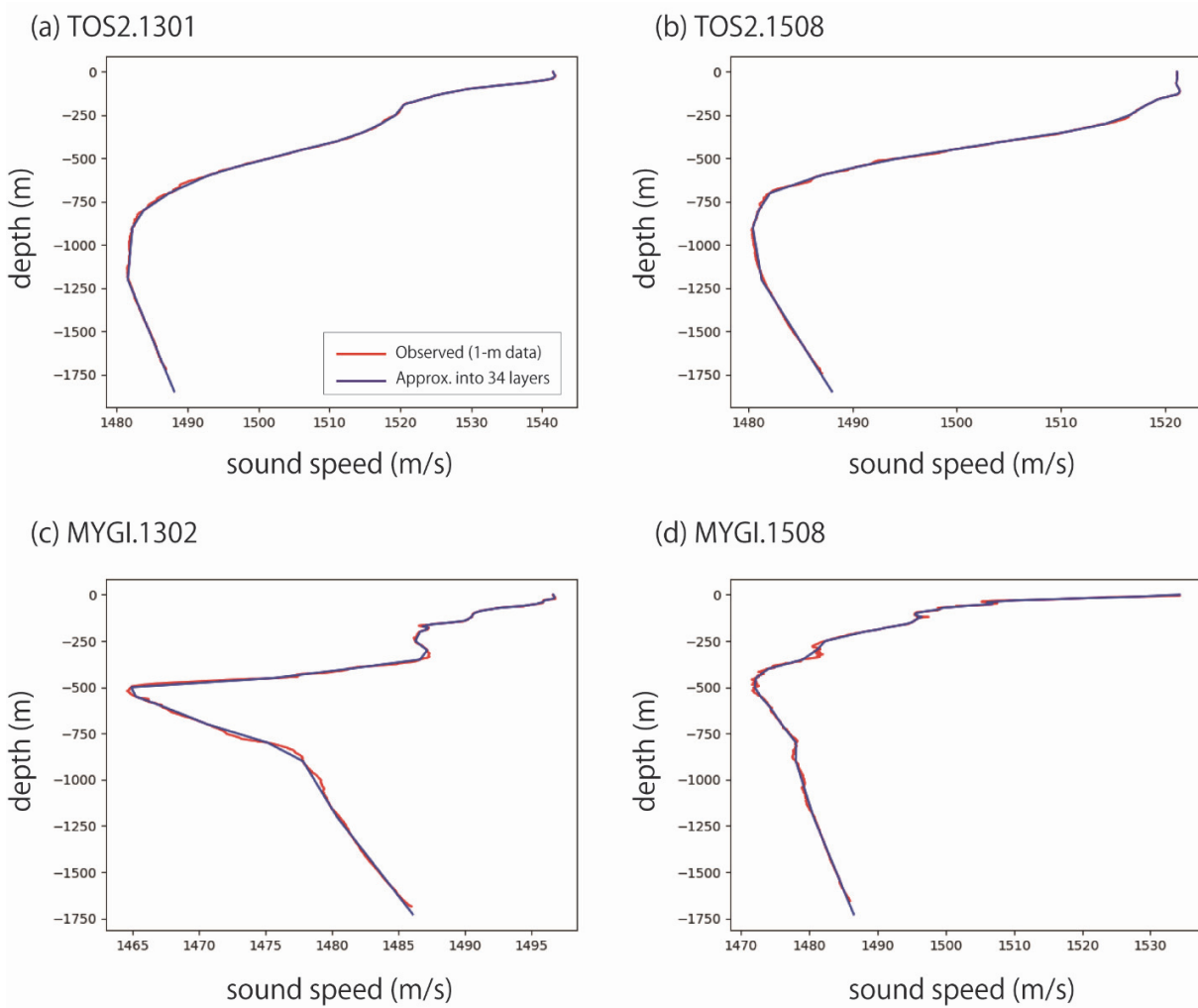
802



803

804 Figure 4. Locations of the tested GNSS-A sites TOS2 and MYGI.

805

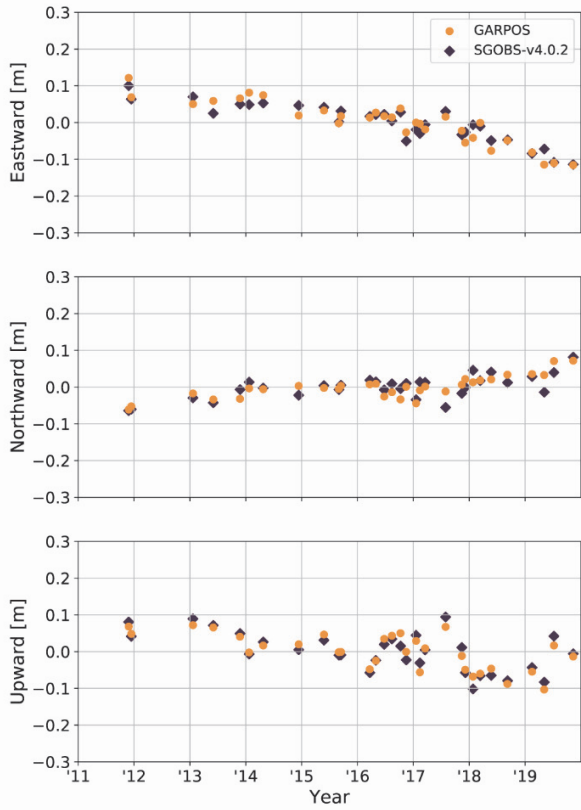


806

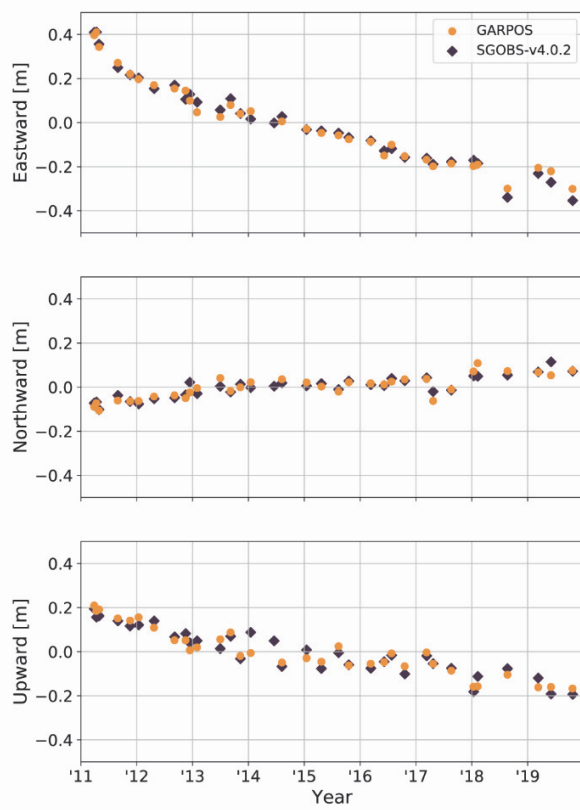
807 Figure 5. Reference sound speed profiles (blue lines) for epochs (a) TOS2.1301 (Jan. 2013), (b)  
 808 TOS2.1508 (Aug. 2015), (c) MYGI.1302 (Feb. 2013), and (d) MYGI.1508 (Aug. 2015). Red  
 809 lines indicate 1-m sound speed profiles obtained from the 1-m layered XBT/XCTD data.

810

(a) TOS2



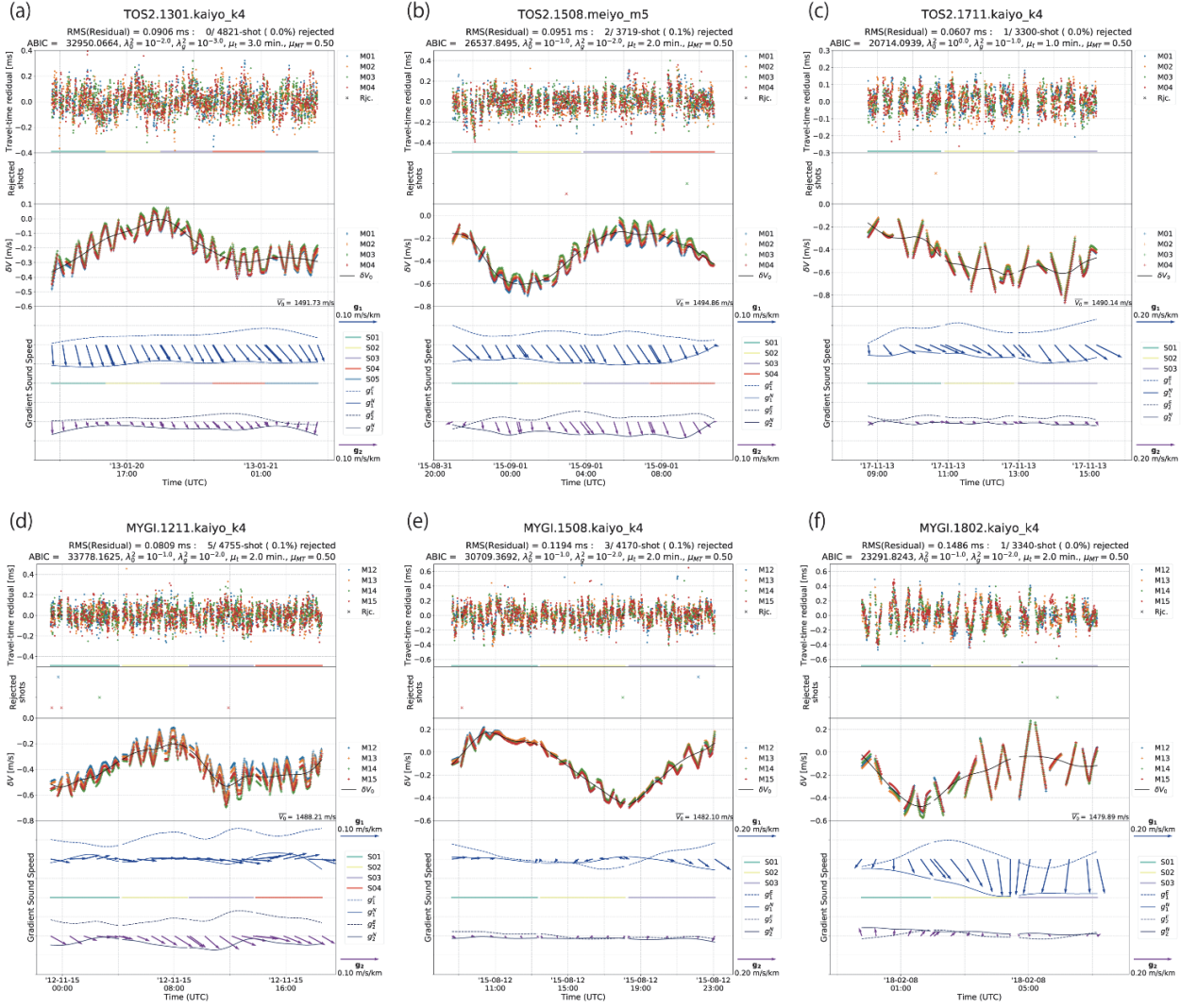
(b) MYGI



811

812 Figure 6. Time series of displacement at (a) TOS2 and (b) MYGI solved by GARPOS (orange  
813 circles) and SGOBS version 4.0.2 (blue squares). The positions are aligned to the ITRF 2014.

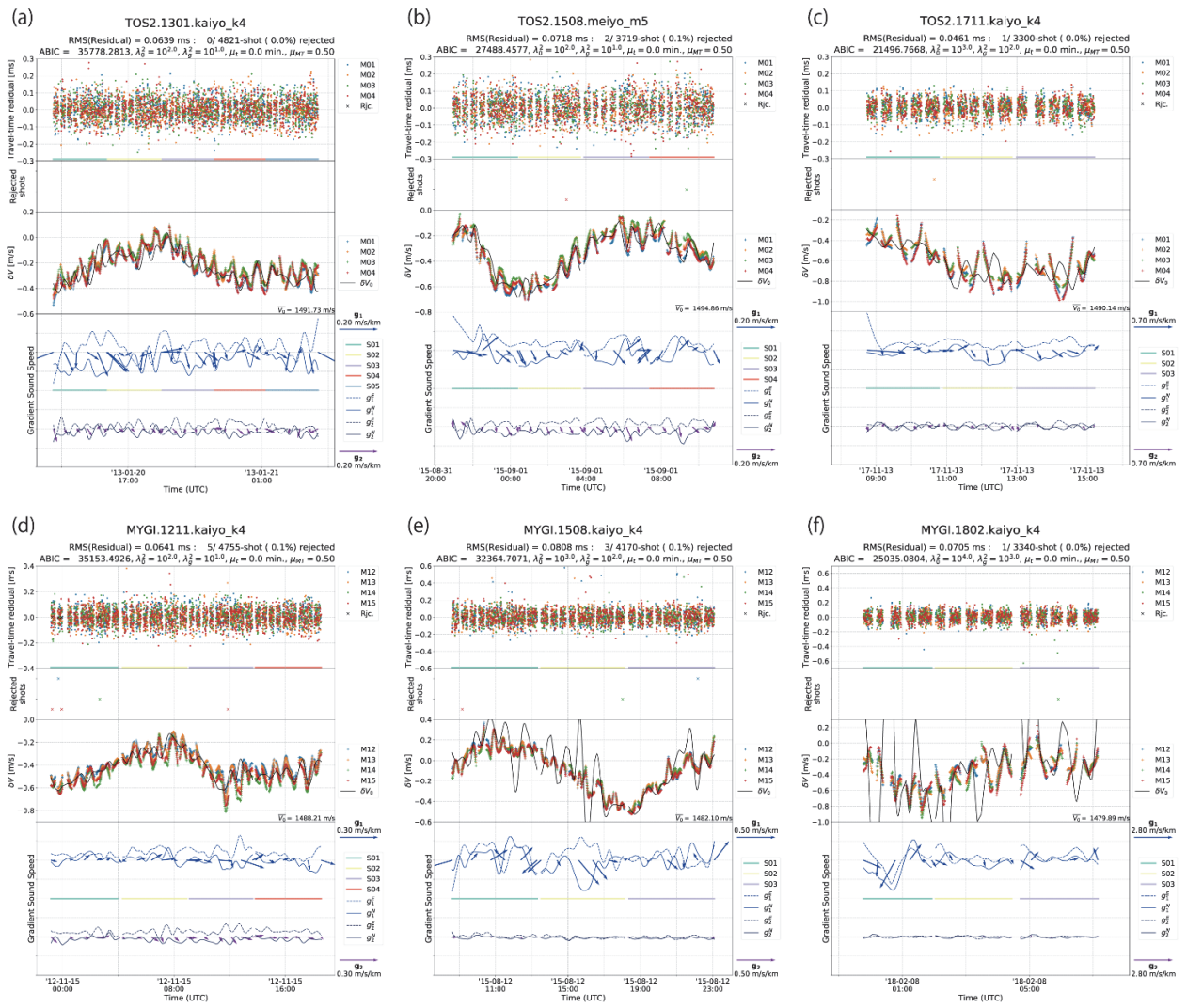
814



815

816 Figure 7. Estimated results of the most preferred model for epochs (a) TOS2.1301.kaiyo\_k4, (b)  
 817 TOS2.1508.meiyo\_m5, and (c) TOS2.1711.kaiyo\_k4 (d) MYGI.1211.kaiyo\_k4, (e)  
 818 MYGI.1508.kaiyo\_k4, and (f) MYGI.1802.kaiyo\_k4. The top panels show the model residuals  
 819 of the round-trip travel time. The second panels show the rejected acoustic data in the  
 820 preprocessing step for determining the array geometry. The third panels indicate the sound speed  
 821 perturbations, i.e.,  $\gamma_i \bar{V}_0$  (the crosses), and  $\delta V_0(t) \equiv \bar{V}_0 \alpha_0(t)$  (black line). The colours of the  
 822 symbols in these panels identify the target transponders. The blue and purple arrows on the  
 823 bottom panels indicate the spatial gradient of the sound speed perturbations in north-up  
 824 expression, i.e.,  $g_1(t) \equiv \bar{V}_0 \alpha_1(t)$ , and  $g_2(t) \equiv \bar{V}_0 \alpha_2(t)$ , respectively. Dotted lines and solid  
 825 lines show the temporal variations of eastward and northward components, respectively. The  
 826 colored horizontal lines denote the ranges of the observation subsets.

827



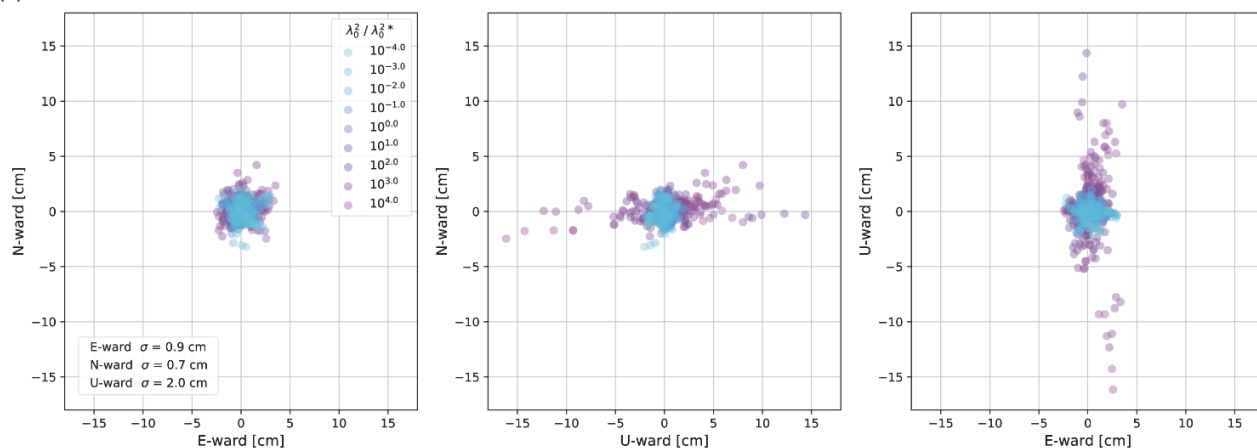
828

829

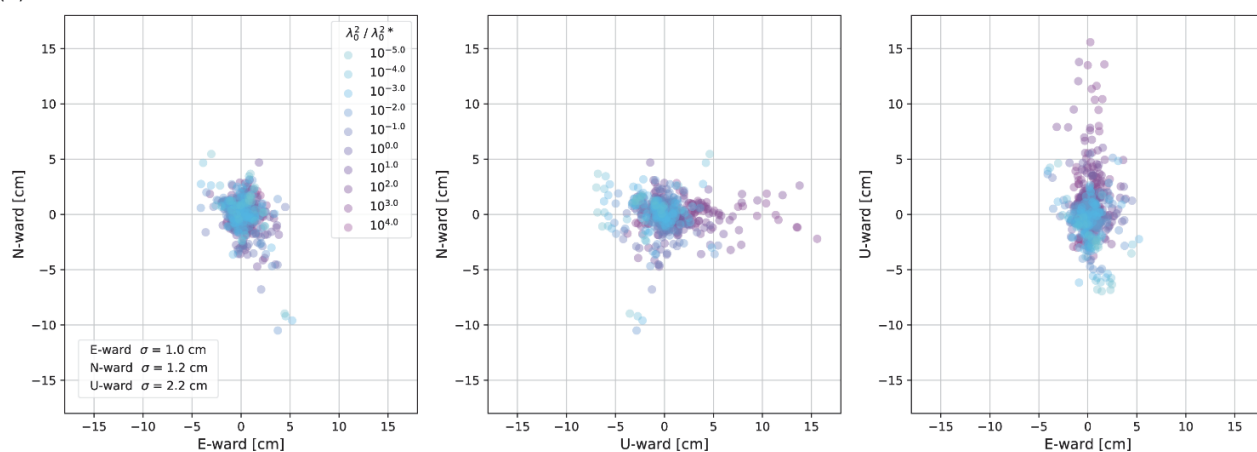
Figure 8. Same as Figure 7, but for the most preferred model in the models with  $\mu_t = 0$ .

830

(a) TOS2



(b) MYGI



831

832 Figure 9. Distributions of differences of positions of the tested models from the preferred ones at (a)  
 833 TOS2 and (b) MYGI for northward-eastward (left), northward-upward (center), and upward-  
 834 eastward (right) components. The colours of circles indicate the value of  $\lambda_0^2 / \lambda_0^{2*}$ .

835

## 836 16 Tables

837 Table 1. List of observable and estimation parameters used in GARPOS.

Parameter	Description	Name in I/O file	I/O file	type	unit
$t_{i+}$	transmit time	<i>ST</i>	I-2	obs	s
$t_{i-}$	reception time	<i>RT</i>	I-2	obs	s
$\mathbf{Q}(t_{i+})$	Position of GNSS antenna at $t_{i+}$ in ENU coordinates	<i>ant_e0</i> <i>ant_n0</i> <i>ant_u0</i>	I-2	obs	m
$\mathbf{Q}(t_{i-})$	Position of GNSS antenna at $t_{i-}$ in ENU coordinates	<i>ant_e1</i> <i>ant_n1</i> <i>ant_u1</i>	I-2	obs	m
$\Theta(t_{i+})$	Attitude of platform at $t_{i+}$	<i>roll0</i> <i>pitch0</i> <i>head0</i>	I-2	obs	deg.
$\Theta(t_{i-})$	Attitude of platform at $t_{i-}$	<i>roll1</i> <i>pitch1</i> <i>head1</i>	I-2	obs	deg.
$\gamma_i$	Correction coefficient	<i>gamma</i>	O-2	est	-
$\mathbf{M}^0$	Prior ATD offset	<i>ATDoffset</i>	I-1	obs	m
$\mathbf{X}_j^0$	Prior position of transponder	<i>M{jj}_dPos</i>	I-1	obs	m
$\Delta\mathbf{X}^0$	Prior offset of transponder array	<i>dCentPos</i>	I-1	obs	m
$\hat{\mathbf{M}}$	Posterior ATD offset	<i>ATDoffset</i>	O-1	est	m
$\hat{\mathbf{X}}_j$	Posterior position of transponder	<i>M{jj}_dPos</i>	O-1	est	m
$\hat{\Delta\mathbf{X}}$	Posterior offset of transponder array	<i>dCentPos</i>	O-1	est	m
$V_0(u)$	Reference sound speed profile	CSV table	I-3	obs	m/s
$K_a$	Number of internal knots for $\alpha_0$	<i>nmp0</i>	I-4	setting	-
$K_b$	Number of internal knots for $\alpha_1$	<i>nmp1</i>	I-4	setting	-
$K_c$	Number of internal knots for $\alpha_2$	<i>nmp2</i>	I-4	setting	-

838 \* Note that  $K_{\begin{smallmatrix} a \\ b \\ c \end{smallmatrix}} = nmp \begin{Bmatrix} 0 \\ 1 \\ 2 \end{Bmatrix} \times (\text{number of subset})$  in GARPOS.

839



840 Table 2. List of hyperparameter in GARPOS.

Hyper-parameter	Description	Formulation set in (I-4)	Name in Setting file	unit
$\mu_t$	Correlation length of data	$\mu_t$	<i>mu_t</i>	min.
$\mu_{MT}$	Data correlation coefficient b/w the different transponders	$\mu_{MT}$	<i>mu_mt</i>	-
$\lambda_0^2$	Smoothness parameter for $\alpha_0$	$\log_{10} \lambda_0^2$	<i>Log_Lambda0</i>	-
$\lambda_{1E}^2$	Smoothness parameter for $\alpha_{1E}$	$\log_{10} \left( \frac{\lambda_{(\cdot)}^2}{\lambda_0^2} \right)$	<i>Log_gradLambda</i>	-
$\lambda_{1N}^2$	Smoothness parameter for $\alpha_{1N}$			-
$\lambda_{2E}^2$	Smoothness parameter for $\alpha_{2E}$			-
$\lambda_{2N}^2$	Smoothness parameter for $\alpha_{2N}$			-
$\sigma^2$	Scale of measurement error	N/A	N/A	-
$\rho^2$	Scale of a priori positioning error	N/A	N/A	m <sup>2</sup>

841 \* Note that  $\sigma^2$  is calculated analytically, and that  $\rho^2$  is set in (I-2).

842 Table 3. Locations and observation periods of the GNSS-A observation sites used in this study.

Site	Latitude	Longitude	Height	Number of epochs	Observation period
TOS2	32.43 °N	134.03 °E	-1740 m	31	2011.904 – 2019.863
MYGI	38.03 °N	142.92 °E	-1640 m	33	2011.238 – 2019.803

843